CREW HaT

Cosmic Radiation Extended Warding using the Halbach Torus

Final Report – NIAC Phase I 2022

February 21, 2024

Principal Investigator	Elena D'Onghia, Ph.D.	Department of Astronomy
Co-Investigator	Paolo Desiati, Ph.D.	Wisconsin IceCube Particle Astrophysics Center
Collaborator	Bryan Bednarz, Ph.D.	Department of Medical Physics
In collaboration with	John Pfotenhauer, Ph.D.	Department of Mechanical Engineering
	Franklin Miller, Ph.D.	Department of Mechanical Engineering
And with	Ziyang Hang	Department of Mechanical Engineering
	Maddy Healey	Department of Mechanical Engineering
	Ohyun Kwon	Department of Medical Physics
	Eric Martin	Department of Mechanical Engineering
	Emil Pellett	Department of Astronomy
	Mikayla Seigal	Department of Mechanical Engineering
	Jack Winter	Department of Mechanical Engineering

Abstract

This report presents the Phase I feasibility study of an open-geometry configuration of superconducting magnets known as the CREW HaT. This technology has the potential to offer a revolutionary solution to protect astronauts from space radiation during long-duration missions. Our study focuses on the ability of these magnets to deflect Galactic Cosmic Rays and Solar Particle Events. It compares their mass, power, and shielding efficiency with conventional passive methods and active shielding methodologies previously proposed.

Through extensive research and analysis, we have identified a promising preliminary design that offers a feasible and imminent advancement for enhancing astronauts' safety on extended space missions. This Phase I report provides detailed information on particle trajectory numerical calculations, superconducting coil design, critical current, coil conductor options, number of turns and layers, supporting mechanical structure design, stability, protection, overall mass, and power requirements.

We have constructed a Monte Carlo computational framework to estimate the radiation exposure dose with arbitrary passive and active configurations and space radiation conditions. With this, we can now compute the whole-body equivalent dose that the mission crew is subjected to in space as a fundamental tool for establishing the environmental requirements for the active shielding system's engineering design.

Based on our findings, an additional passive shielding layer provides equivalent mitigation to our active shielding system at a considerable mass cost. Our study has identified challenges to investigate and has produced the information and tools necessary to proceed to the next iteration, where we will address the CREW HaT feasibility under stricter conditions.

Overall, we believe that the CREW HaT represents a significant advancement in space radiation shielding technology that will play a crucial role in ensuring the success of future interplanetary missions.

Table of Contents

1. Introduction

In this new era of American space exploration, NASA is gearing to return astronauts to the Moon by December 2025, marking this generation's first crewed lunar landing [1]. This mission is expected to lead to extended lunar stays, and the eventual establishment of Artemis Base Camp is just the opening chapter. The ultimate frontier, however, lies in the human exploration of Mars, a challenge that hinges on overcoming a critical obstacle: the health hazards posed by cosmic radiation. The most concerning space radiation in cislunar and interplanetary space consists of solar particle events and galactic cosmic rays.

Solar Particle Events (SPE), primarily electrons, protons, and other ions with energy up to a few 100 MeV/n, originate from solar flares and coronal mass ejections, particularly during periods of maximum solar activity. The burst events can last hours to days with intense particle flux but relatively low energy. Conversely, Galactic Cosmic Rays (GCR) particles consist of a relatively low flux of particles, primarily protons, but with relevant contributions of heavy ions. The GCR particles reach 1,000 GeV/nucleon energies and above, as shown in Figure 1.1.

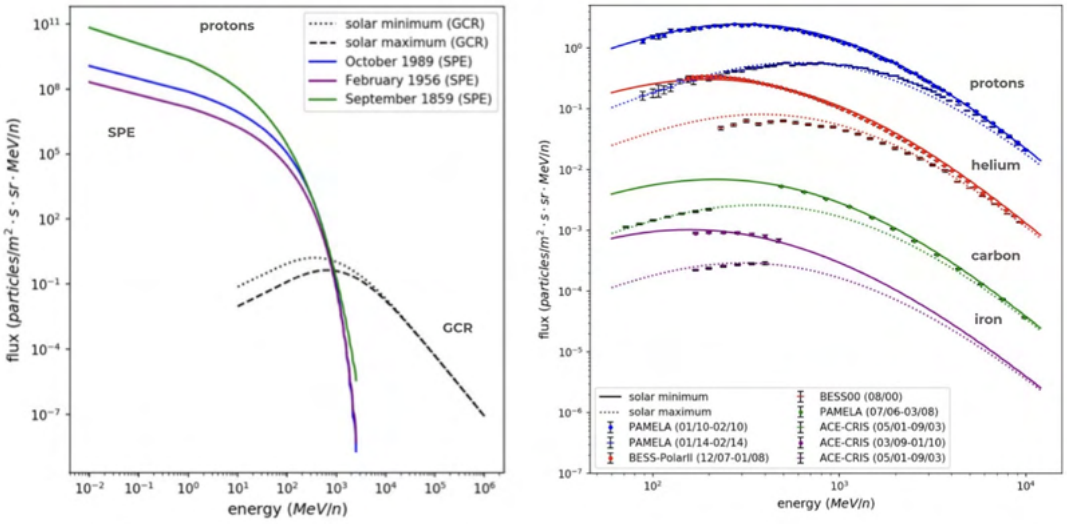

Figure 1.1: *Left* – Energy distributions of three selected SPE event occurrences compared with GCR flux. *Right* – Energy distribution of GCR particles (H, He, C, Fe) experimentally observed (symbols) and the fluxes corresponding to the measurement dates according to the Badhwar-O'Neill 2014 model [36] (lines). (Courtesy: High School Science Research Internship.)

The figure shows that the eleven-year solar cycle modulates the GCR flux. During Solar Minimum, GCR particles can penetrate easily through the quieter heliosphere, resulting in higher flux. During Solar Maximum, the enhanced solar wind activity and turbulence partially shield us from the incoming GCR particles, thus reducing the flux by a factor of three and exposure by roughly a factor of two compared to Solar Minimum, depending on shielding [4]. At the same time, the frequency of SPE events increases during the solar maximum epochs [2].

Protecting astronauts from cosmic radiation is a critical concern for space exploration. The Earth's magnetic field is a natural protective cocoon, shielding our planet from harmful

space radiation, including SPE and GCR particles. Although still within the natural Earth's magnetosphere, astronauts on the International Space Station (ISS) receive already radiation doses from space between 80 and 160 mSv per 6-month mission [2, 3]. A standard medical chest X-ray delivers approximately 0.1 mSv, and the average annual dose or exposure from GCR radiation on Earth's surface is 0.34 mSv/year, corresponding to 10% of a person's yearly exposure due to all-natural radiation sources [5]. The dose equivalent from GCR exposure on the Moon's surface is about 1.4 mSv/day with no shielding during the 2019 solar minimum [6].

A natural magnetic shield is absent in free space – the destination for extended missions to the lunar surface and Mars. Hence, long-duration exposure to high-energy GCR and SPE poses severe health risks, including damage to the central nervous system, skin, gastrointestinal tract, skeletal system, and blood-forming organs [7]. This risk factor sets the standard for setting radiation limits for male and female astronauts at different ages using estimates above the 95% confidence level (CL) for uncertainties in risk projection models [4]. Uncertainties related to predicting particle energy spectra and the limited understanding of heavy-ion radiobiology lead to uncertainty that requires extra margin when setting radiation limits. Although inconclusively, there is a 3% excess risk of death from cancer at a cumulative dose of 1000 mSv [4, 8], just below the 1200 mSv dose expected from a three-year round trip to Mars.

On Earth, mitigating radiation exposure encompasses a combination of passive shielding and distance, which is challenging to employ in space. NASA has set specific recommendations for radiation mitigations for missions beyond low Earth orbits [7]. Mitigations against SPE bursts rely on space weather forecast warnings, upon which the crew can take shelter during the burst. Cargo reconfiguration or dedicated passive-shielded shelters in the spacecraft are sufficient to absorb the relatively low energy of SPE particles. GCR shielding requirements are more complex due to the difficulties arising from their slowly varying flux and high-energy and high-Z characteristics. The recommendations for space habitats to provide protection from GCR include the reduction of GCR exposure during Solar Minimum (i.e., the worst-case scenario) by 15% compared to free space, such that the effective dose from GCR remains below 1.3 mSv/day in open space and below 0.8 mSv/day on planetary surfaces. For missions longer than 600 days, an additional mitigation strategy requires a lifetime exposure limit of 600 mSv [7].

An additional mitigation strategy relies on the natural GCR modulation driven by the solar cycles. NASA estimations concluded that exposure from GCRs could be reduced by approximately a factor of 2 by timing Mars missions during periods of Solar Maximum. However, the eleven-year solar cycle's predictions have uncertainties of about 2.8 years, significantly reducing the launch window to meet the 600-mSv exposure limit of only six months. Reducing the uncertainty in the solar cycle duration by half will increase the launch window by a factor of 4 [2, 7]. However, even a smaller solar cycle length uncertainty will significantly impact estimates of solar activity projected in the next 20 years, making it challenging to establish the best window of opportunity for a three-year Mars mission.

Beyond health concerns, cosmic radiation can disrupt spacecraft systems and electronics, a critical consideration for mission success. Therefore, developing effective radiation mitigation strategies is paramount for the safety and feasibility of long-duration space

exploration beyond the Moon and poses the question of exploring new shielding technologies [7].

There are two approaches to protecting spacecraft and astronauts from the harmful effects of space radiation: passive and active shielding. With passive shielding, space radiation is absorbed through a layer of material. It is the mitigation currently adopted in space. Any material can stop ionizing particles up to a specific energy, above which they penetrate the shield [9]. For instance, an aluminum slab with 2, 4, and 10 cm thickness (corresponding to a mass thickness of approximately 5, 11, and 27 g/cm^2, respectively, which is the product of the density, 2.7 g/cm^3, and thickness) can stop protons up to about 50, 70, 125 MeV [10]. Passive shielding may work for high-Z GCR particles at energies below 1 GeV/n. However, while losing energy penetrating the habitat's walls, GCR particles induce nuclear collisions and fragmentations, generating lower energy secondary particles, including gamma rays and neutrons [11], which are harmful to biological tissues. Therefore, the crew inside the habitat faces this internal mixed radiation environment risk.

Another problem is the excessive mass needed to achieve acceptable radiation mitigation. Polyethylene is a good shielding material because it has high hydrogen content and hydrogen atoms efficiently thermalize neutrons and absorb radiation [9, 12-19]. However, better solutions may exist for a long-term space mission (e.g., Mars) [20, 21]. An example of passive shielding is the one suggested for the Artemis mission to ensure the safety of future space crews traveling to the Moon by producing well-fitted vests to wear in space [22, 23]. While low-cost and lightweight, the vests are designed to protect vital human organs from radiation. Although this solution might work for the softer SPE particles, it has negligible protection from the more energetic GCR and secondary debris. As a result, it is inadequate to shield humans in long-haul missions to Mars.

The most promising approach to protect the crew from cosmic radiation is generating a magnetic field surrounding the spacecraft, similar to Earth's magnetosphere. Feasibility studies showed that this strategy is superior to any passive shielding approach in terms of efficiency in reducing the impact of radiation on spacecraft. However, mass and power consumption are critical to the practical realization of such future devices [9, 24-28]. Compared to the large and heavy closed magnetic field systems studied in the past [7, 24, 25], open magnetic field concepts, more similar to the Earth's magnetic field, show promise to be a lighter-weight solution with a significantly lower impact surface for secondary radiation production [9]. The challenge for an open magnetic field geometry is to achieve the best compromise among mechanical structure weight, strength to support the intense magnetic forces and crew safety. The challenge lies in optimizing the geometry of the open magnetic shielding to achieve a tradeoff between the structure bulk and the strength to support the intense magnetic forces while managing the cost of the necessary superconducting magnets. The success in navigating these technical hurdles will be pivotal in ensuring the safety of astronauts on their journey to Mars.

2. Feasibility Study Strategy for CREW HaT

This study explores the feasibility of an open-geometry active magnetic shielding concept to protect astronauts from GCR radiation during long-haul space missions. The study consists of closely linked investigations into various aspects of the problem. The magnetic field must be strong enough to repel GCR particles back into space while being weak or virtually non-existent in the crew habitat. We developed a pioneering concept based on Halbach Arrays [30] to realize this objective.

The Cosmic Radiation Extended Warding (CREW) magnetic shield concept uses a cylindrical Halbach array arrangement called Halbach Torus (HaT) [29]. This system comprises eight electromagnet coils arranged around the habitat region with rotating magnetic polarities (shown in Figure 2.1), which generate a magnetic field that extends in space around the CREW HaT while suppressing the magnetic field in the habitat region at the center.

Figure 2.1: Rendering of the CREW HaT active magnetic shielding concept attached to SpaceX Starship's crew habitat.

This concept can be significantly lighter than the previous closed-geometry configurations adapted to similar-sized spacecraft. It achieves this by using a sparse support structure that reduces the target for GCR particles to collide and produce harmful secondary neutral particles. The challenge with this concept is to develop the ability to produce a sufficiently high magnetic field density and withstand generated magnetic forces.

This report outlines the investigation strategy followed in our Phase I study. The strategy consists of interconnected components. Firstly, numerically calculate GCR particle trajectories in the CREW HaT's magnetic field for a given geometry configuration, such as coil shape, size, distance from the spacecraft's surface, and total electric current in each coil. Our milestone was to find the geometry configuration that provides at least 50% GCR proton

flux reduction at 600 MeV on the spacecraft. This step provided us with a *geometry configuration benchmark* we used to design the electromagnetic coils and support structure.

Secondly, use the configuration benchmark's total current and geometry to design a superconducting coil with optimal conductor winding geometry capable of producing the required magnetic field. Evaluate the self-induced magnetic forces to design the enclosing case to keep the conductor in place. Estimate the resulting coils' mass and assess all safety issues and cryo-cooling power consumption acceptable for long-haul space travel necessary for high-temperature superconducting coils operations.

Thirdly, use the total current and coil arrangement geometry to evaluate the inter-coil magnetic forces, investigate the requirements for the choice of materials, design an initial support mechanical structure capable of counteracting the forces, and maintain the coils in place. Then, evaluate the minimal total mass necessary to produce the required magnetic field with the chosen geometry configuration benchmark constraints.

In addition, assess the whole-body equivalent dose absorbed by the spacecraft crew without and with the CREW HaT active shielding and compare it with the effect of additional passive shielding equivalent mass that would produce the same exposure reduction as the active shielding.

Finally, use the radiation dose estimation to re-iterate the initial geometry configuration and total current to converge towards a configuration that satisfies the NASA requirements on radiation exposure during extended space missions with manageable total mass and power consumption. The process may include, e.g., geometry modifications (different coil shapes) and the addition of passive shielding to mitigate active shielding mass, safety, and power consumption.

This report marks the completion of Phase I in our investigation into the requirements for superconducting coils and their support structure. The insights gained from this study guide our next steps and highlight the challenges we face moving forward. Our initial analysis centered on developing a magnetic shield to protect a typical Lunar Gateway habitat from cosmic radiation, serving as a preliminary benchmark [29]. This feasibility assessment is situated within the framework of a prospective three-year journey to Mars, envisioning the use of SpaceX Starship's 9-meter diameter and a habitat volume that remains to be determined. The exact volume of the habitat and the interior layout remain undetermined at this stage. Considering the Starship's size, the CREW HaT configuration in this report is considerably larger than the benchmark system in [29], adjusting our scope to match the ambitious scale of interplanetary travel. This approach ensures that we are preparing for a range of possibilities, ready to adapt our designs to meet the challenges of human space exploration.

3. Particle Shielding Evaluation

We know that the Earth's magnetosphere is capable of shielding our planet's surface by diverting GCR particles back into space. Its quasi-dipolar structure, with field strength at Earth's surface varying between 0.25 and 0.65 Gauss (corresponding to 25-65 μTesla), shields against protons below 1 GeV in the polar regions and below about 20 GeV in the equatorial regions, thus reducing the GCR flux at the top of the atmosphere. Such a naturally generated magnetic field protects planetary surfaces from the deleterious effects of GCR particle radiation. The extraordinary shielding power of Earth's magnetosphere against 1-10 GeV particles is due to its vast extension across tens of thousands of km into space. In order to provide the same shielding at a distance scale of 10 m, we would need a magnetic field similar to Earth's configuration but with strength approximately $(6\times10^6/10)^3$ times larger. To shield a spacecraft from GCR particles, we can only grossly approximate the efficiency of Earth's magnetosphere. We do not need to reproduce the highly efficient geomagnetic shielding power, but enough to allow a three-year return mission to Mars and keep the crew safe.

3.1 Particle Trajectory Numerical Calculation

We use the CREW HaT geometry concept described in Section 2 to evaluate the magnetic field's effectiveness in diverting electrically charged particles away. The Halbach array shown in Figure 3.1 surrounds the spacecraft at a radial distance $R_{Halbach}$ related to the radial dimension of the spacecraft $R_{sc} = 4.5\ m$ (assuming SpaceX Starship) and the radial extent of the individual coils $R_{coil,OD}$ according to the relation $R_{Halbach} \geq R_{sc} + R_{coil,\ OD}$. Equation (3.1) defines the aspect ratio (AR) for elliptically-shaped coils, where $R_{major} \geq R_{minor}$. Note that AR = 1 implies that the coils' shape is circular.

$$AR = \frac{R_{major}}{R_{minor}} \tag{3.1}$$

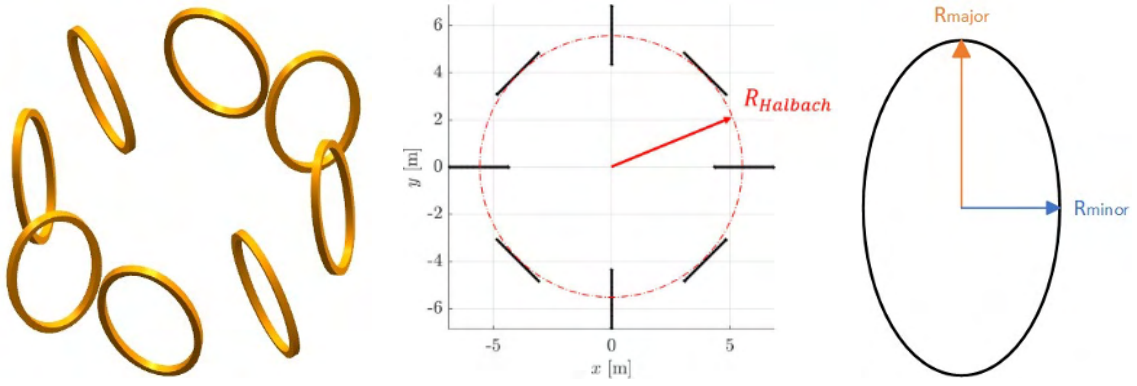

(a) Halbach array (b) Top view (c) View of one coil

Figure 3.1: Geometric representation of the CREW HaT in an isometric view (on the left) and top view (on the center) and view of an ellipse coil (on the right).

Using this geometry, we evaluate the magnetic field generated when an electric current flows through each of the eight coils. The magnetic field from each coil at any point in space is calculated using the Biot-Savart law

$$\vec{B}(\vec{r}) = \frac{\mu_0}{4\pi} \int_{Coil} \frac{I\, d\vec{l} \times \vec{r}}{|\vec{r}|^3} \tag{3.2}$$

providing the magnetic field generated by the current I in a wire element $d\vec{l}$ at a distance $\vec{r}$. The integral is along the coil (here assumed with infinitesimal thickness). The constant $\mu_0 = 4\pi \cdot 10^7$ N/A^2 is the permittivity in vacuum. Figure 3.2 shows the generated magnetic field.

Particles with electric charge q moving in a magnetic field $\vec{B}$ at velocity $\vec{v}$ are subject to the Lorentz force

$$\vec{F} = q\,\vec{v} \times \vec{B} \tag{3.3}$$

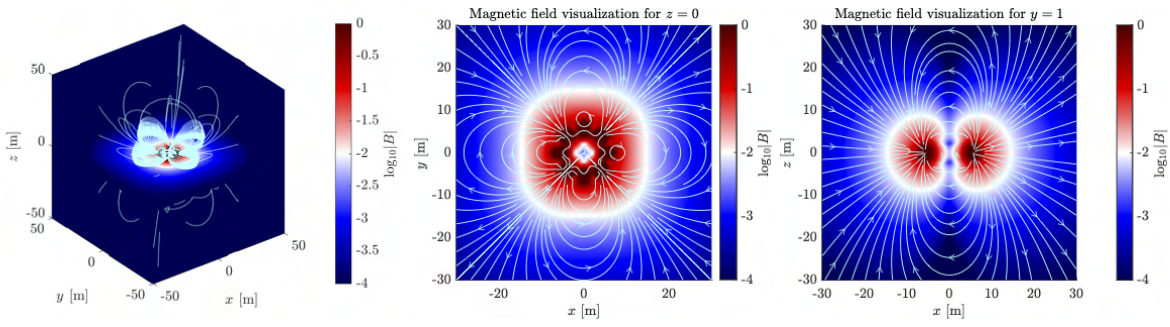

Figure 3.2: Representation of the CREW HaT magnetic field lines and strength (color scale). *Left* – 3D view. *Center* – projection perpendicular to the spacecraft's axis. *Right* – projection along the spacecraft's axis [35].

We calculate proton trajectories by employing a Monte Carlo generation of random initial positions $\vec{r}_0$ on a sphere of 100 m radius and random momentum vectors $\vec{p}_0$ towards the inner sphere. The trajectories are then numerically advanced using the 4th Order Runge-Kutta stepping function until they pass through the magnetic field and move outward into open space. An adaptive time step algorithm is used to maintain numerical accuracy in the varying magnetic fields generated by the CREW HaT. We calculate the trajectories of several thousands of protons at different energies (from 1 MeV to 10 GeV) and record their closest approach to the geometric center of the system.

The trajectories approaching the center point within 4 m are considered "hit" (i.e., they hit the spacecraft habitat) and are indicated in red in Figure 3.3. We define transmission probability as the ratio between the number of particles reaching the spacecraft habitat (i.e., the red trajectories in Figure 3.3) and the number of incident particles from space. A transmission probability of 0% means perfect shielding.

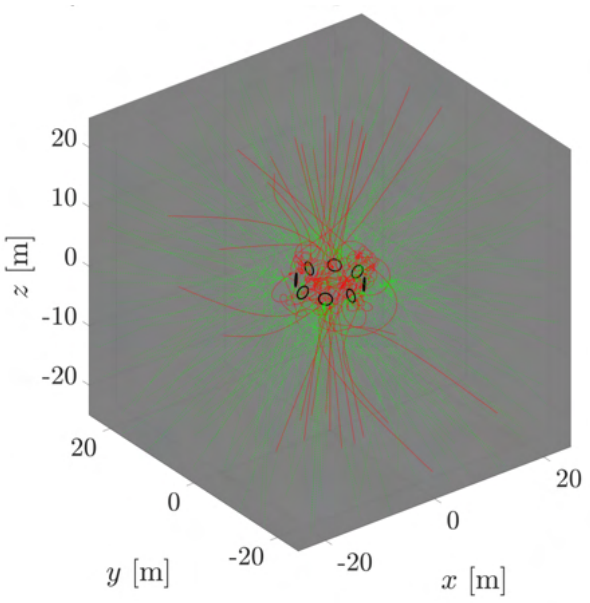

Figure 3.3: Visualization of protons interacting with the magnetic field. Particle trajectories that "hit" the spacecraft are colored red; deflected trajectories are colored green [35].

Ultimately, the transmission probability is determined by the extent and magnitude of the magnetic field generated by the Halbach array. In addition to the size and shape of the coils, the field profile and strength depend on the location of the eight coils, particularly their distance from the spacecraft and the total operating current passing through the coil winding. Limitations to the operating current within the high-temperature superconductors (see Section 4) and commercially available piece lengths dictate the size and shape of the winding pack, limiting how close the coils can be to the spacecraft. Considering these various constraints, a parametric study has been carried out to assess the transmission probability as a function of the operating current, the distance of the coils from the spacecraft, and the size and shape of the coils. Given the aforementioned constraints, the goal is to reduce the number of GCR trajectories hitting the spacecraft's habitat (i.e., the red trajectories in Figure 3.3) as much as possible. The CREW HaT does not have an effective magnetic field shielding for GCR particles coming through the magnetic field "caps." In the future, we will investigate how to provide effective mitigations in that regard, possibly involving additional passive shielding.

Figure 3.4 displays the transmission probability associated with the magnetic field from eight elliptical coils in the Halbach array with an 8 m radius (i.e., the coils' center distance from the spacecraft's axis) and various values of applied current. The test current varies from $4 \cdot 10^6$ amperes to $1 \cdot 10^7$ amperes with a step of $2 \cdot 10^6$ amperes in our parametric study. An applied current of $1 \cdot 10^7$ amperes produces a transmission probability close to 50% when the proton energy is 600 MeV, which was our Phase I initial requirement. In Figures 3.5 – 3.7, r_H is the Halbach radius $R_{Halbach}$, and r_{coil} represents R_{major} as measured at the center of the winding pack. Figure 3.5 displays the transmission probability for various combinations of coil geometry and Halbach radii with the same applied current of $1 \cdot 10^7$ amperes.

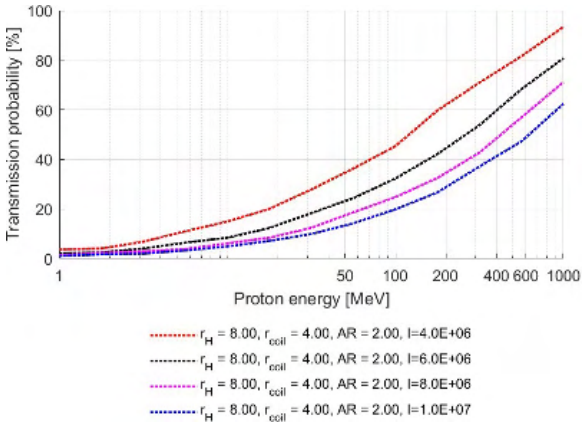

Figure 3.4: Proton transmission probability for elliptical coils (AR=2) with different applied total electric currents.

Note from Figure 3.5 that elliptical coils with the $r_{coil} = 4$ m and AR = 2 have a very close performance to that provided by circular coils with a radius of 3 m for Halbach radii of either 7 m or 8 m. Therefore, both elliptical and circular coils can provide acceptable shielding.

Two additional cases are displayed in Figure 3.6 and Figure 3.7, showing the influence of the coil size and shape on the transmission probability while holding r_H constant at 8 m. For all cases except one, the current is also held constant at $1 \cdot 10^7$ amperes. Figure 3.6 also reveals that to maintain a proton transmission probability of about 50% for 600 MeV while using an elliptical coil with a semi-major radius of 3.5 m and aspect ratio of 2, the total operating current of the coil would need to be increased to $1.2 \cdot 10^7$ amperes. Alternately, holding the total current at $1 \cdot 10^7$ amperes for an elliptical coil with a semi-major radius of 4.5 m and aspect ratio of 2, the transmission probability for 600 MeV radiation is decreased below 45%.

The results shown in Figure 3.7 reveal that a circular coil with an operating current of $1 \cdot 10^7$ amperes must have a radius (to the middle of the winding pack) of at least 3 m to provide a shielding probability as low as 50%.

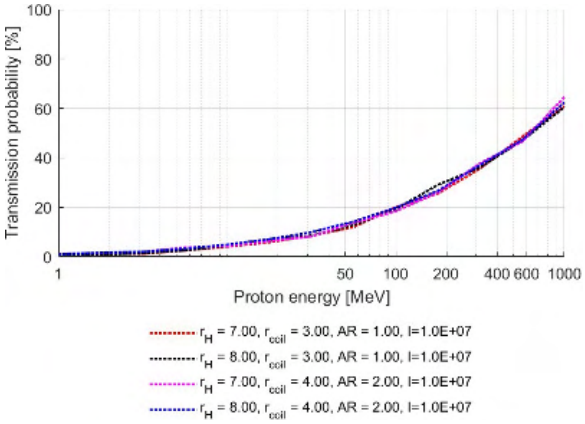

Figure 3.5: Proton transmission probability for elliptical (AR=2) and circular (AR=1) coils with different geometric parameters.

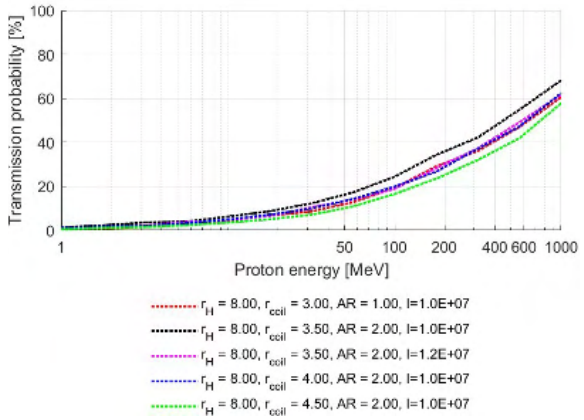

Figure 3.6: Proton transmission probability for elliptical (AR=2) and circular (AR=1) coils with different coil dimensions.

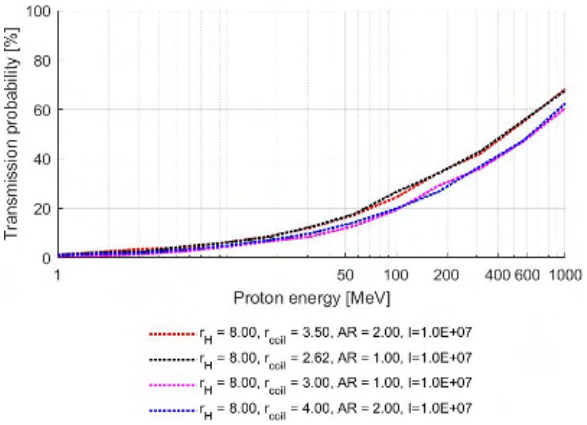

Figure 3.7: Proton transmission probability for elliptical (AR=2) and circular (AR=1) coils with different coil shapes.

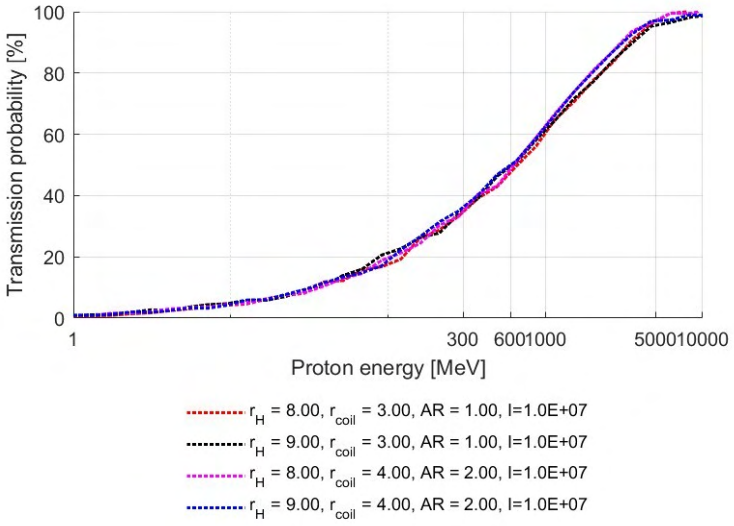

Figure 3.8: Proton transmission probability up to 10 GeV.

Figure 3.8 shows the proton transmission probability across the full range of energy where the shielding efficiency drops to zero (around 10 GeV/n).

Section 6 of this report describes the Monte Carlo calculations that we have used to estimate the whole-body equivalent dose that an astronaut could be exposed to in deep space. To perform these calculations, we have simulated the flux of different GCR particles using the Badhwar-O'Neill 2014 model [36]. Different particle trajectories in magnetic fields are identical as long as they have the same Larmor radius at all times during their motion. Therefore, to compute the transmission probability for an arbitrary GCR particle with atomic (mass, number) = (A, Z), we scale the energy using the proton transmission probability of Figure 3.8 to maintain the same Larmor radius

$$R_L = \frac{|\vec{p}_\perp|}{qB} = \frac{Amc^2}{ZeBc}\sqrt{\left(\frac{E_{kin}}{Amc^2} + 1\right)^2 - 1}\,, \tag{3.4}$$

where E_{kin} is the particle's kinetic energy. As an example, in the high-energy limit ($E_{kin} \gg Amc^2$), the Larmor radius is invariant if the particle's kinetic energy scales as E_{kin}/Z (also known as "rigidity"). For instance, a proton with an energy of 10 GeV has the same trajectory geometry as a 260 GeV Iron nucleus propagating in the same magnetic field.

3.2 Geometry Configuration Benchmark

Our parametric study of the transmission probability as a function of the operating current, the distance of the coils from the spacecraft, and the coils' size and shape led us to select a geometry configuration benchmark.

Geometry Parameter	Value
$R_{Halbach}$	8 m
R_{major}	4 m
AR	2
I	$1 \cdot 10^7$ amperes

Table 3.1: Geometric parameters of the CREW HaT configuration benchmark.

We used this benchmark to develop an initial feasibility study encompassing the superconducting coil design (Section 4) and the support mechanical support structure (Section 5). The key aspect relating the geometry configuration to the engineering design is the forces exerted by the CREW HaT magnetic field on the current bearing coil.

The Lorentz force from equation (3.3) exerted on a charged particle moving in a magnetic field can also be expressed as the force on a wire segment $d\vec{L}$ with current I

$$d\vec{F} = Id\vec{L} \times \vec{B}. \tag{3.5}$$

Section 4.2 provides a detailed description and computation of the magnetic forces induced by each coil on itself. These forces act externally on the plane of the coil, resulting in hoop stresses. The design of the coil's casing must ensure minimal movement within the winding pack, and that expansion under the influence of the hoop stress is accounted for.

The inter-coil magnetic forces are approximately an order of magnitude smaller than self-induced forces because of the larger distance between the coils. However, they are essential to the coil pack design (Section 4) and the mechanical support structure (Section 5).

Figure 3.9 schematically shows the inter-coil magnetic forces on each CREW HaT's coil with self-induced Lorentz force contributions removed. The four coils facing the axis of symmetry experience a complex load distribution resembling a Pringles chip's shape. The remaining four coils have a radially inward force component. This suggests that a large portion of the force the CREW HaT superstructure feels will be directed inwardly. The complex loading must be handled effectively with the structural design, as shown in Section 5.

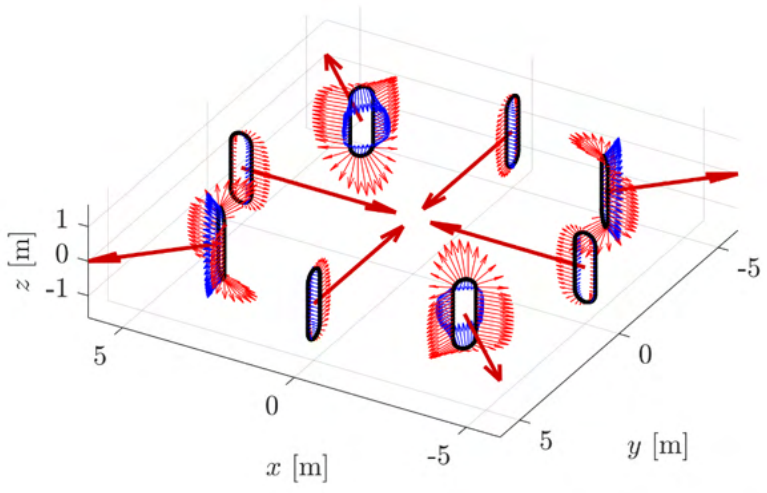

Figure 3.9: Intercoil forces (light red) and net force (dark red) on each coil in the Halbach array [35].

4. Superconducting Coil Design

4.1 Executive Summary

The design process for each of the eight identical coils making up the CREW HaT Halbach array is summarized here. Details of the various steps and supporting analyses are provided in the subsequent sections of this chapter.

Beginning with the requirements for effective shielding, at least 50% GCR proton attenuation at 600 MeV, the required total current tracing through the coil's winding pack is fixed at $1 \cdot 10^7$ amperes (see Section 3.1). Furthermore, following a variety of considerations, the size and shape of each coil have been reduced to two options: an elliptical solenoid with semi-major and semi-minor radii of 4 m and 2 m, respectively, and a circular solenoid with a radius of 3 m.

The combination of total current and coil size results in a peak magnetic field of 10 Tesla on the inner winding of the coil pack. Analytical and numerical methods have been used to confirm this maximum field strength.

High-temperature superconducting (HTS) tapes have been selected to generate the magnetic field. These are available, for example, from the SuperPower Company [31] in the form of Yttrium Barium Copper Oxide (YBCO) superconducting tapes with a thickness of 1 mm and widths from 4 mm to 12 mm. The maximum current that the tapes can carry in their superconducting state depends on the operating temperature as well as on the magnitude and direction of the magnetic field at the surface of the tape. An operating temperature of 40 K has been selected as this design point. At the same time, the direction of the magnetic vector at the surface of the tape on the inner winding was determined via the use of the numerical code Maxwell, the electromagnetic package within the commercial software product ANSYS [32]. Based on the temperature and the magnetic field vector, the operating current for the 4 mm wide tape is 80 amperes. To provide the total current of $1 \cdot 10^7$ amperes, the winding pack built from the 4 mm tape must, therefore, include 125,000 turns. Alternate configurations have been investigated, including a 12 mm wide tape and a cabled 48-tape Conductor on Round Core (CORC) arrangement available from the Advanced Conductor Technologies company [33].

HTS coil wounds using tape conductors are typically either pancake or layer wound [34]. Based on the maximum piece lengths that are commercially available (900 m for a single YBCO tape and 800 m for a single CORC cable), the maximum distance around the perimeter of the coil, and the typical structure required for joints between the pieces, a layer-wound configuration with joints positioned on the outer turns of each layer is selected to use. The average number of turns per layer for the 12 mm wide tape is 40, resulting in a required number of layers corresponding to 1042.

Conductors carrying current in the presence of a magnetic field are subject to a Lorenz force, which results in a radial outward force in the case of a solenoid (Section 3.2). We used the Maxwell software package to determine the magnitude and direction of the self-induced Lorenz forces on each coil. The associated tensile stress induced on the HTS tape greatly

exceeds its yield strength. To support the forces and avoid conductor motion within the winding pack, a co-wound layer of high-strength, low-weight material is chosen for each turn of the tape conductor. Two materials satisfying the strength requirements are Kevlar and a Carbon-fiber reinforced composite.

Concerns regarding conductor “thermal” stability were examined. Considering the remote possibility that the YBCO layer within the tape would crack, thereby disrupting the current flow through the superconductor and locally generating heat, a 48-tape CORC has been examined and selected as the preferred option for the HTS element.

As a result of the number of turns for the coil wound with the single YBCO tape, the size of the Halbach coils, and the operating current, each coil stores a large amount of energy, 5.35 MJ. The associated inductance of the coils, 98 Henries, is also large. The inductance is highly dependent on the number of turns. Using the CORC tape rather than the single 12 mm wide tape reduces the number of turns from 125,000 to 2,632, and the inductance is reduced from 98 Henries to 0.74 Henries. Both features will significantly impact any protection plan for the coil that would guard against a thermal runaway failure condition. Although various superconducting magnet protection systems have been identified, these will require further investigation.

The total mass of the coils has been calculated by summing the mass of the various components. Coil configurations that provide the required magnetic field while minimizing mass have a mass per coil of approximately 15 tons, resulting in a combined mass of slightly over 120 tons for all eight coils. Phase II activities are envisioned to investigate ways to reduce the mass. These include 1) grading the magnet, 2) replacing the copper core of the CORC conductor with aluminum, and 3) developing a range of coil-mass values as a function of the appropriate range of shielding values (up to 200 mSv/yr) and key related parameters such as the maximum required magnetic field.

Three candidate cryogenic cooling systems have been identified to provide the necessary cooling to maintain the superconducting coils at 40 K. The required cooling capacity is based on estimates of the heat load from three sources: solar radiant heat incident on the coils, resistive heat generated from the many conductor joints, and heat generated in the current leads to each coil. The total estimated heat load of about 190 watts exceeds the currently available cooling capacity of the candidate cooling systems by a factor of four. Phase II efforts will explore methods to both decrease the heat load on the coils and increase the cooling capacity of the candidate cooling systems.

4.2 Analysis tools

The CREW HaT shielding system consists of eight identical superconducting coils that comprise the Halbach array and create a strong magnetic field to deflect high-energy charged GCR particles in space. The high current passing through the superconducting coils generates the magnetic field, whose strength will depend on the applied current in the coils and the geometry and configuration of the coils. Therefore, a thorough analysis of the winding geometry for one of the eight identical superconducting coils has been conducted. Two primary tools are utilized to carry out the magnetic analyses. The first is closed-form

equations, primarily as provided by Iwasa [34], and the second is the numerical code Maxwell, a module of the software package ANSYS [32].

The Biot-Savart law (equation 3.2) is frequently used to calculate the magnetic field along the axial direction of a current loop or solenoid. As shown by Iwasa [34], a generalized version of equation (3.2) for solenoids of arbitrary aspect ratio $\beta = b/a_1$ and thickness $\alpha = a_2/a_1$ can be expressed as

$$B_z(0,0) = \mu_o \lambda J a_1 F(\alpha, \beta) \tag{4.1}$$

As shown in Figure 4.1, a_1, a_2 and b are the inner radius, outer radius, and half-length of the solenoid, respectively, λJ is the overall current density, and F is the geometric "field factor" for the solenoid.

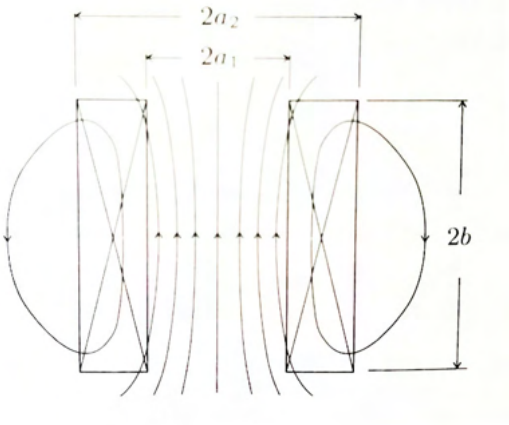

Figure 4.1: Cross-sectional view of a solenoidal coil winding [31].

It is important to notice that equation (4.1) provides only the field in the axial or z direction at the center of the coil. Although values for the field in the axial direction at z = 0 and at other radii may also be calculated via closed-form equations, no such solutions exist to determine the radial field component at arbitrary locations away from the center of the geometrically shaped coil. Information regarding the magnitude and direction of the field within the winding is required to determine the maximum current that HTS tapes can carry. Calculating the field strength and direction at arbitrary locations from the center of a solenoid requires numerical codes. The present study extensively uses the electromagnetic code Maxwell, which is available within the software package ANSYS [32].

4.2.1 ANSYS Maxwell

Simulating the magnetic field is the first step to performing the required analyses of a single coil within the CREW HaT array. The ANSYS Maxwell software package simulates the magnetic field of the single coil and can mesh and simulate the field in three dimensions. Figure 4.2 shows the mesh of a single elliptical coil generated by ANSYS Maxwell.

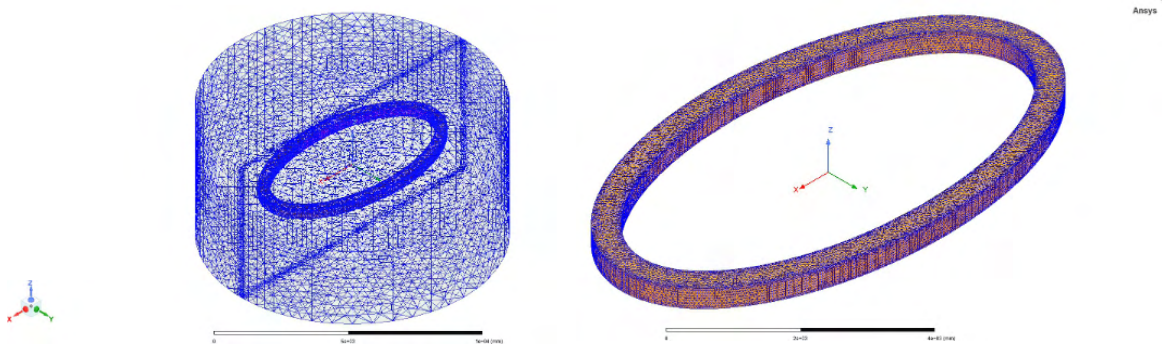

Figure 4.2: ANSYS Maxwell mesh for a single elliptical coil. *Left* – Mesh including boundary. *Right* – Mesh without boundary.

Maxwell uses the Finite Element Method (FEM) as a numerical tool for magnetic field analysis. The results for the superconducting coil within the Halbach array include the magnetic field's strength and orientation. Conducting a mesh-sensitivity and boundary-sensitivity study is necessary to produce reliable results. As usual, if too many small-sized meshes are generated for the research object, the cost in time and memory usage can be prohibitively high. As a result of the mesh optimization study, we found that 1.5 million meshes with a maximum length of 100 mm and a symmetrical cylindrical boundary with a radius of 6 m and a height of 6 m are the best settings for the modeling analysis. Detailed information regarding the optimal mesh settings is listed in Table 4.1. Figure 4.3 displays a sample of information generated by Maxwell for a single coil within the Halbach array.

For the results shown in Figure 4.3, the elliptical coil has a semi-major of 4 m, a seminar of 2 m (see Section 3.2), a height of winding pack in the axial direction of 0.43 m, and a thickness of winding pack in the radial direction of 0.34 m. It is made with 41,667 turns of a 12 mm wide YBCO tape with around 240 amperes of applied current. Surrounding the coil is a 12m × 6 m cylindrical vacuum boundary. Note that, as shown here, the maximum field occurs at the z = 0 location of the inner winding of the coil.

Setting Objects	Setting Parameters
Maximum Mesh Length	100 mm
Curved Surface Meshing	Fine/Large
Maximum Number of Passes	17
Minimum Number of Passes	15
Minimum Converged Passes	15
Refinement Per Passes	15 %
Percent Error	1
Maximum Number of Meshes	1.5 million
Minimum Number of Meshes	1 million

Table 4.1: ANSYS Maxwell optimized mesh settings.

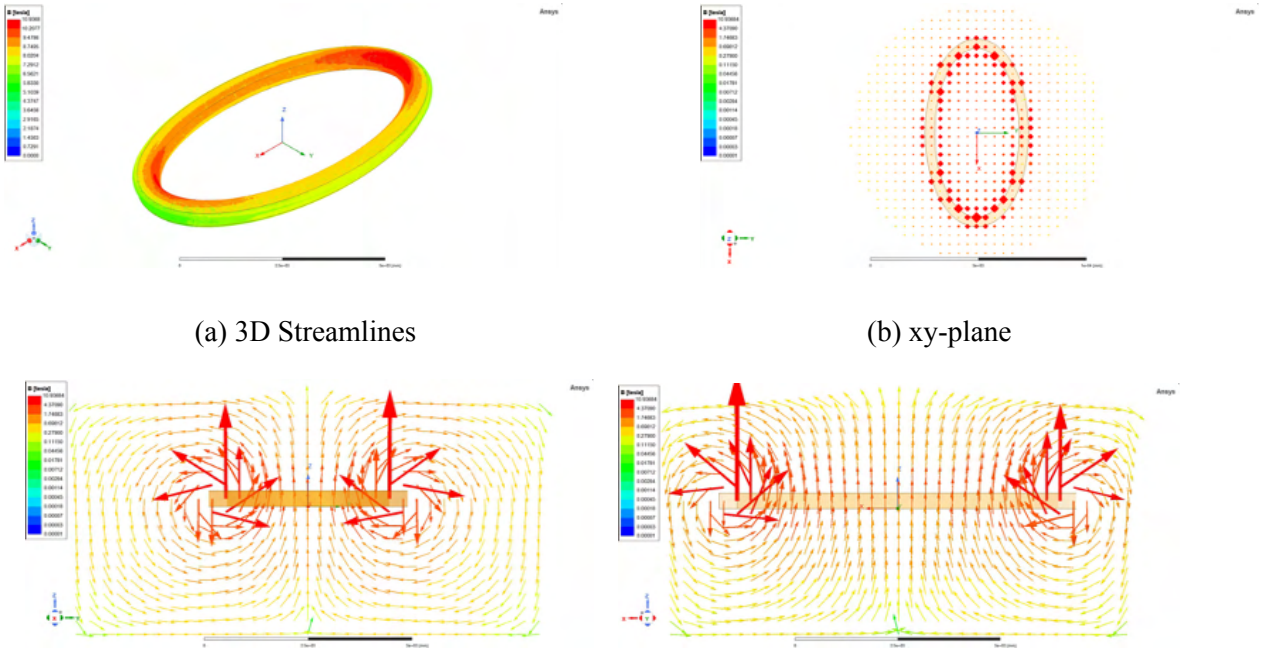

(a) 3D Streamlines (b) xy-plane

(c) yz-plane (d) xz-plane

Figure 4.3: ANSYS Maxwell numerical representation of the magnetic field lines of an elliptical coil. a) magnitude of flux density along the winding, b) magnitude of flux density at various x-y locations perpendicular to the coil axis, c) magnitude and direction of flux density on the x=0, yz plane, d) magnitude and direction of flux density on the y=0, xz plane.

4.2.2 Closed-Form Equations

In addition to the magnitude and direction of the magnetic field generated within the winding of the superconducting magnet, it is also necessary to account for the associated magnetic forces. Thousands of superconducting tape turns are wound together to make up each Halbach array's coil, each subject to a local Lorentz force. Figure 4.4 shows the analytical solution for the Lorentz force per unit length between two parallel current-carrying wires. Here, the current flowing through each wire in the presence of the magnetic field generated by the current flowing in the other wire results in the Lorentz force. For the case of a solenoid, the current flowing in each turn, in the presence of the field generated by the multiple windings, produces a net Lorentz force directed radially outward as well as an attractive force between adjacent conductors. The net radially outward Lorentz force is equivalent to a magnetic pressure p_m that scales as

$$p_m = \frac{B_o^2}{2\mu_o}, \tag{4.2}$$

where B_o is the axial magnetic field's strength at the center of the magnet. The hoop stress associated with the magnetic pressure and acting on each winding turn is one of the important factors calculated in this study. In addition to the scaling factor given in equation (4.2), the

hoop stress within the magnet winding varies with the aspect ratio, length of the coil, and location within the coil. The Maxwell package provides the factor given in equation (4.2) but cannot account for the aspect ratio and length of the coil. Nevertheless, Figure 4.5 shows the stress analysis determined by Maxwell at the internal surface of an elliptical coil with major and minor radii of 4 m and 2 m, respectively, and carrying $1 \cdot 10^7$ amperes.

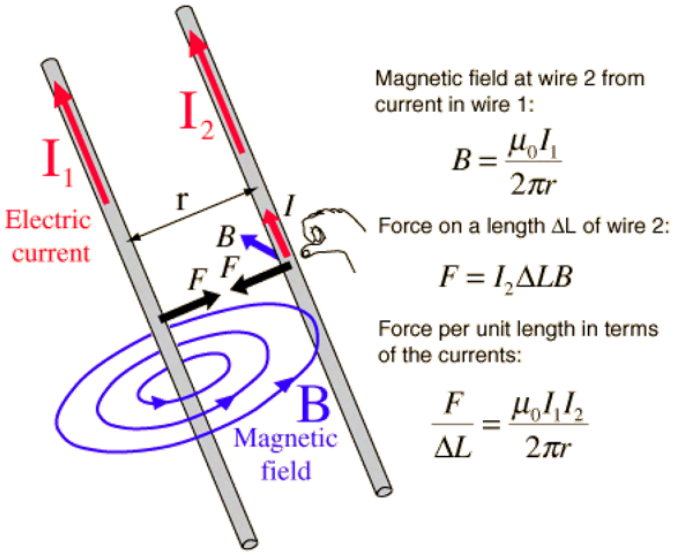

Figure 4.4: Magnetic force between parallel wires of unit length L.

Although the stress analysis results with Maxwell do not account for the aspect ratio, Figure 4.5 is still informative. It shows the direction and distribution of the stress at the internal surface of the coil. For an elliptical coil, the hoop stresses are not uniform as the magnetic field strength is largest at the ends of the ellipsoid (see Figure 4.3).

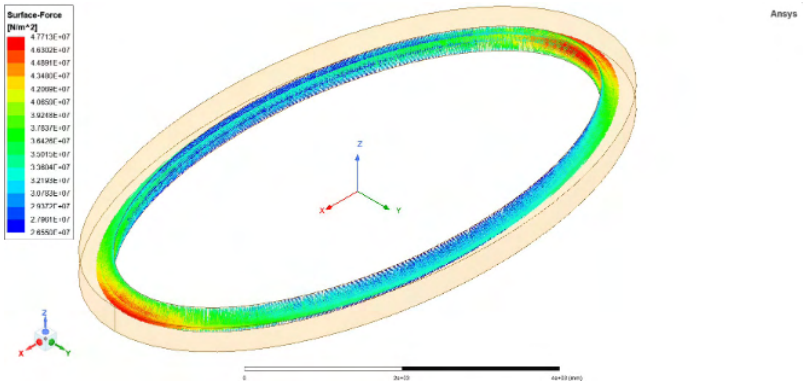

(a) D Streamlines

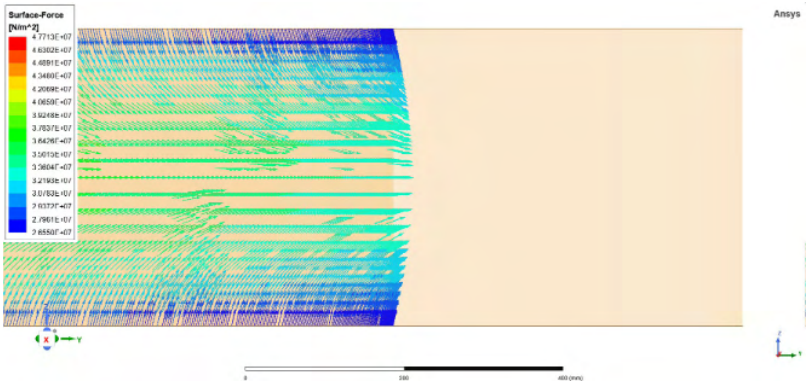

(b) yz-plane

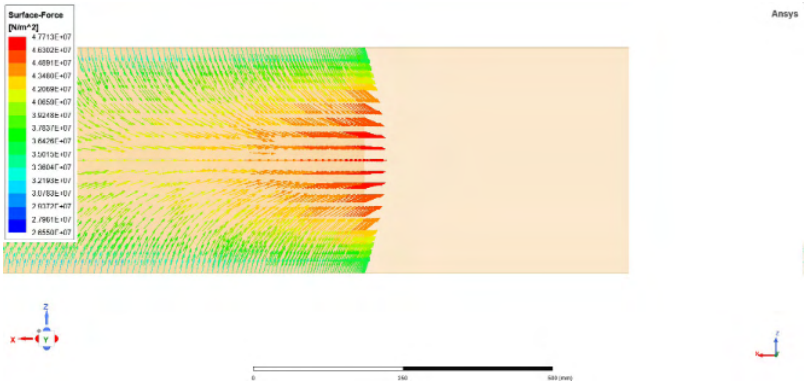

(c) xz-plane

Figure 4.5: Internal surface force density of the single coil.

The equations determining the radial and hoop stresses as a function of the aspect ratio and length of an isotropic solenoid are provided by Iwasa [34]. Equations 4.4 and 4.5 display the radial and hoop stress for the isotropic coil with a winding current density of λJ, where λ is the "space factor," accounting for the non-current-carrying portion of the coil's cross-section. Two dimensionless parameters are defined as $\kappa = \frac{B_2}{B_1}$ and $\rho = \frac{r}{a_1}$. The axial magnetic field varies linearly with r, so $B_z\ (r = a_1) = B_1$ and $B_z\ (r = a_2) = B_2$, where $a_1 \leq r \leq a_2$. The parameters a_1 and a_2 are as depicted in Figure 4.1. All subsequent analyses of the hoop stress internal to the coil use equations 4.3 and 4.4.

$$\sigma_\rho = \frac{\lambda J B_1 a_1}{\alpha - 1}\left[\frac{2+\nu}{3}(\alpha - \kappa)\left(\frac{\alpha^2+\alpha+1-\frac{\alpha^2}{\rho^2}}{\alpha+1} - \rho\right) - \frac{3+\nu}{8}(1 - \kappa)\left(\alpha^2 + 1 - \frac{\alpha^2}{\rho^2} - \rho^2\right)\right] \quad (4.3)$$

$$\sigma_\theta = \frac{\lambda J B_1 a_1}{\alpha - 1}\left\{(\alpha - \kappa)\left[\frac{2+\nu}{3}\left(\frac{\alpha^2+\alpha+1+\frac{\alpha^2}{\rho^2}}{\alpha+1}\right) - \frac{1+2\nu}{3}\rho\right] - (1 - \kappa)\left[\frac{3+\nu}{8}\left(\alpha^2 + 1 + \frac{\alpha^2}{\rho^2}\right) - \frac{1+3\nu}{8}\rho^2\right]\right\} \quad (4.4)$$

4.3 Shape, Applied Current, and Dimensions of Coils

As mentioned in Section 3.1, the design requirement for effective shielding is to produce at least 50% attenuation of the GCR proton flux at 600 MeV. Codes developed in-house [35] utilize the magnetic field generated by the Halbach array to calculate the GCR proton flux attenuation at different particle energies due to the CREW HaT shielding system. The present section explores the proton transmission probability presented in Section 3 as a function of the coil's shape and size and the applied total current.

An interesting design challenge associated with superconducting winding is that the maximum operating current depends inversely on the magnetic field at the location of the conductor. Although, in general, a higher magnetic field enables a more compact winding and, therefore, less required mass and conductor length, the peak field and maximum current are interrelated. Even though the field generated by the winding linearly increases with the operating current, the maximum current that still enables the conductor to be superconducting decreases as the field increases. Thus, optimization typically includes a margin of safety for the operating current to maintain its superconducting state.

As shown in the subsequent section, the operating current influences the geometrical features of the winding pack, which impacts the dimensions of the Halbach array. Thus, the details of the winding pack, the coil size and shape, the applied current, the dimensions of the Halbach array, and the GCR flux attenuation are interrelated, requiring an overall design process that is iterative.

4.4 Coil Shape

A variety of issues have been considered to direct the selection of the basic coil geometry. Prior designs [29, 35] incorporated a race-track geometry for each of the coils in the Halbach array. However, concerns regarding radial conductor motion within the straight sections of the racetrack coils, regardless of the tension used during the winding process, have driven the present preference for either circular or elliptically shaped coils. A thorough analysis of these two coil geometries and their effects on the field generated by the entire array will follow. The advantages and disadvantages of each choice are highlighted.

The magnetic field generated by each coil and the array depends on the coils' geometry. The two basic coil shapes, shown in Figure 4.6, are initially investigated to compare the influence of their shape and size on the magnetic flux density generated in the region surrounding each individual coil. Simulations are carried out using the Magnetostatic module of the Maxwell software package. All coils are modeled with an applied current of $1 \cdot 10^7$ A. Copper is chosen as the coil material, and the surrounding medium is modeled as a vacuum. The resulting plots (Figures 4.7 and 4.8) show in detail the logarithm (base 10) of the magnetic field flux density in units of Tesla.

(a) Elliptical shape (b) Circular shape

Figure 4.6: The different coil geometries investigated.

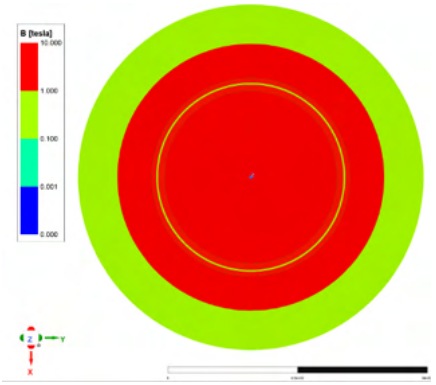

Figure 4.7: Log plot of magnetic flux density of the circular coil.

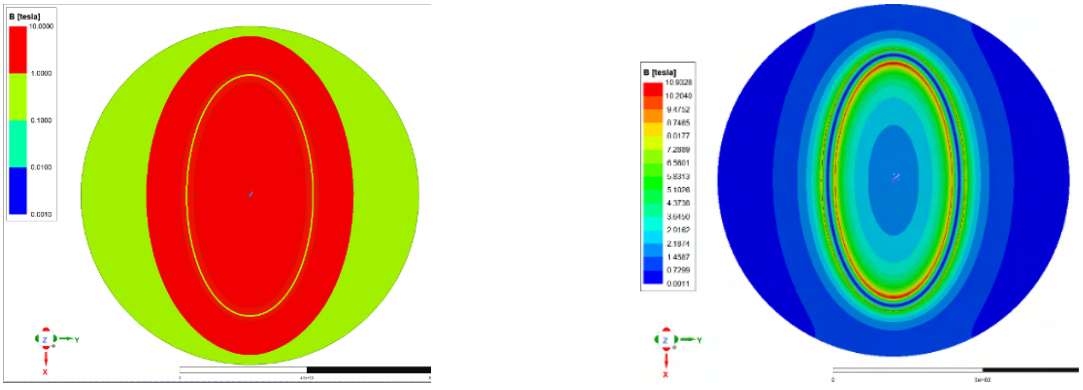

(a) Log plot (b) Linear plot

Figure 4.8: Plot of magnetic flux density of the elliptical coil.

4.4. Circular Coils

The simplest geometry considered for the superconducting coil is a circular shape. In this case, the inner radius of the coil is 3 m. Both the magnetic flux density shown in Figure 4.7 and the magnetic pressure shown in Figure 4.9 reveal an axisymmetric profile with uniform

values around the perimeter at any radial distance from the coil's center. Furthermore, the peak magnetic flux density and pressure values are located at the coil's internal surface. In other words, no field or stress concentrations exist at any azimuthal location around the coil.

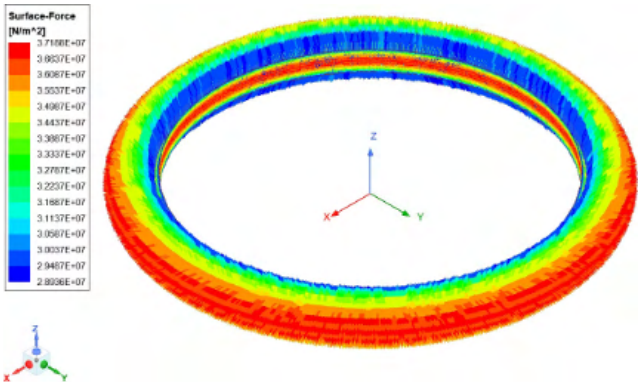

Figure 4.9: Magnetic pressure of the circular coil.

4.4.2 Elliptical Coils

The magnetic flux density and corresponding magnetic pressure for an elliptical coil with semi-major and semi-minor radii of 4 m and 2 m respectively are shown in Figures 4.8 and 4.10. Here, the magnetic flux is not uniform along the coil edge. A higher magnetic field appears along the inside of the ends, as shown in Figures 4.8a and 4.8b. Similarly, Figure 4.10 shows that the magnetic pressure is also concentrated at the ends of the elliptical coil.

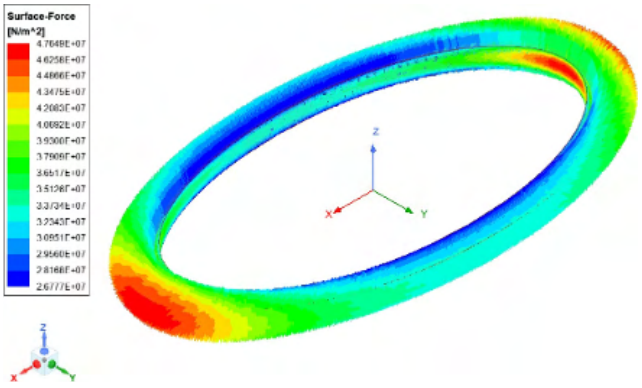

Figure 4.10: Magnetic pressure of the elliptical coil.

The uneven distribution of the magnetic field and magnetic pressure in the elliptical coil can cause some design difficulties. The critical current of the superconducting is dependent on the maximum magnetic field in the coil. In elliptical coils, the peak magnetic field is around 11T, appearing on the internal surface of coils at the ends. The higher field at the ends imposes a lower limit on the maximum current that the HTS can carry throughout the coil. Consequently, more turns will be required to generate the field. Similarly, a higher strength

supporting geometry is needed for elliptical coils to hold the winding pack together compared with that required for the circular coils because of the larger Lorentz forces at the ends of the elliptical coils.

Although the elliptical coil presents design difficulties, it also provides some advantages. In terms of magnetic shielding, the higher aspect ratio of the elliptical coils would be aligned with the spacecraft's longitudinal axis. Such an orientation may provide greater protection along the direction of the spacecraft than circular coils. With eight elliptical coils forming a CREW HaT system, the radius of the Halbach array can be reduced compared to that of an array of circular coils by aligning spacecraft with the long axis of the coils.

4.5 Critical Current

The operating conditions for Niobium-Titanium (NbTi) superconductors as a function of temperature, magnetic field, and current density are visualized in Figure 4.11.

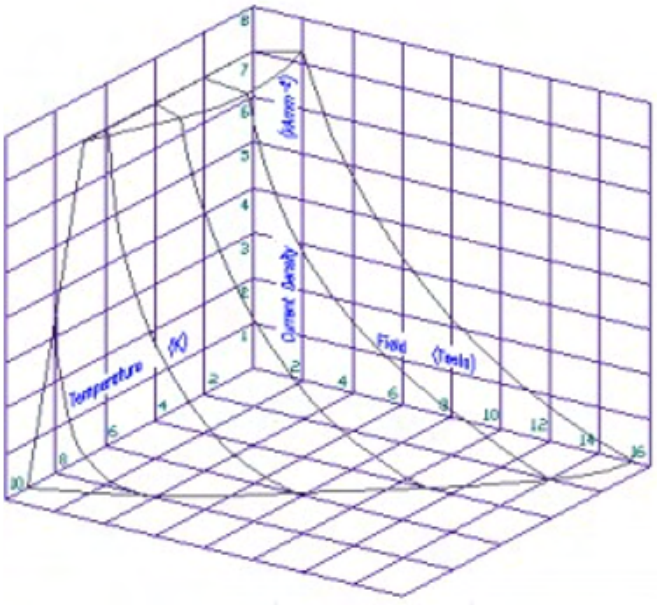

Figure 4.11: NbTi Superconducting Properties [35].

As mentioned, for the present application, YBCO (Yttrium Barium Copper Oxide, YBa2Cu3O7) is chosen as the primary superconducting material because it is commercially available, has a high critical temperature T_c, and a high critical current density J_c when exposed to strong magnetic fields. Superconductivity is destroyed if the applied current in the tape surpasses J_c. The relationship between temperature, magnetic field, and current density for YBCO is visualized in Figure 4.12.

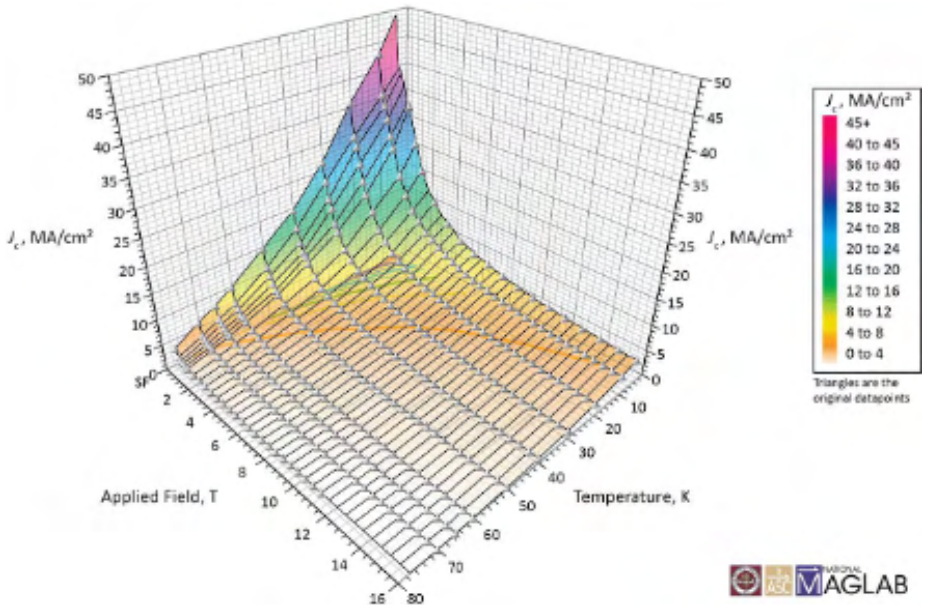

Figure 4.12: Critical current surface for YBCO tape with a magnetic field parallel to the wire [37].

SuperPower Inc. manufactures different widths of YBCO tape from 3 mm to 12 mm that are compatible with the design requirements for CREW HaT [38]. It is essential to note that YBCO tape exhibits a significant dependence of its critical current on both the magnetic field strength and on its orientation relative to the a-b plane of the tape. Due to the manufacturing process, the a-b plane is essentially the same as the plane of the tape. Figure 4.13 shows the critical current I_c as a function of the magnetic field oriented parallel to the a-b plane (a) and perpendicular to the a-b plane (b) for several temperature ranges. Here, the "Lift Factor" is defined as the ratio of the critical current in the presence of an applied magnetic field at some temperature less than 77 K to that under conditions of self-field at 77 K. In all cases, the critical current is significantly reduced for magnetic fields perpendicular to the a-b plane as compared to those when the magnetic field is parallel to the a-b plane.

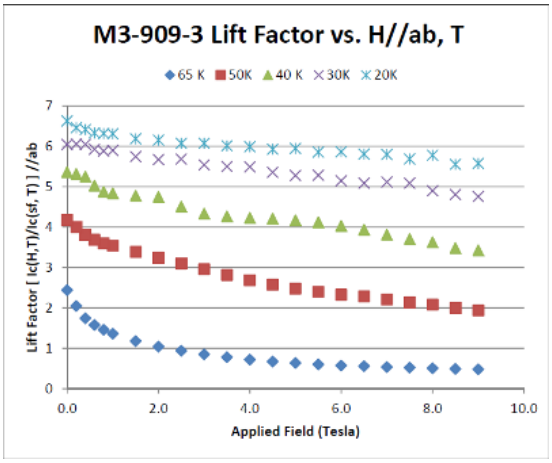

(a) Field parallel to the a-b plane of the YBCO

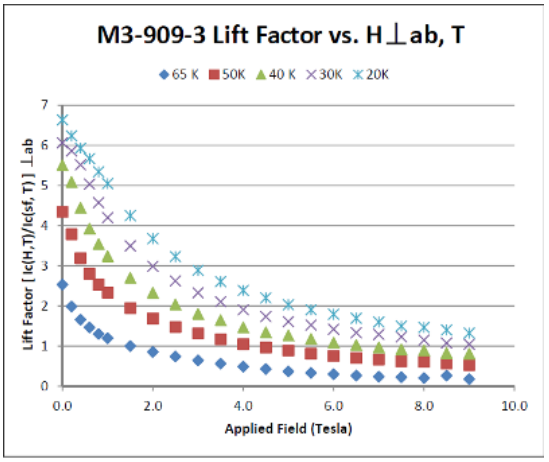

(b) Field perpendicular to the a-b plane of the YBCO

Figure 4.13: Lift Factor vs. applied field at various temperatures [39].

Figure 4.14 was experimentally developed for YBCO tape with a width of 4 mm and with the magnetic field perpendicular to the a-b plane. CREW HaT's coils are designed to operate at a temperature of 40 K and with a maximum magnetic field of around 10 T [29, 35]. Following the 10 T line intersection with the 40 K curve for the operating temperature in Figure 4.13, the critical current I_c for 4 mm YBCO tape is around 100A.

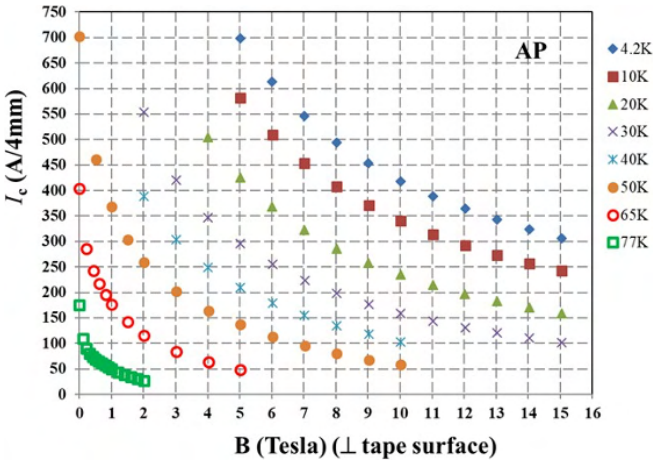

Figure 4.14: Magnetic field dependence of critical current of a 4mm wide AP tape at various temperatures with the field in the direction perpendicular to the tape surface [38].

Figure 4.15 displays the critical current of the 4 mm YBCO tape vs. field angle at 40K and 5T. The field is perpendicular to the a-b plane at 0˚, and it is parallel to the a-b plane at 90˚, where the tape would have a peak critical current of 560 amperes. The minimum critical current happens when the field angle varies between 20˚ to 60˚, which is about 80% of the critical current at 0˚.

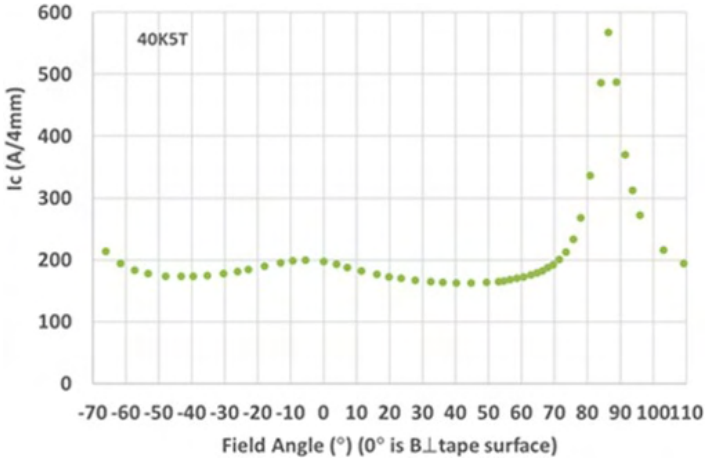

Figure 4.15: Critical current changing with field angles for the 4mm YBCO tape [38].

Figure 4.16 shows the results from the Maxwell package of the field angle within the winding pack. At the edge of the winding pack, the field angle varies from 45˚ to 56˚ from the a-b plane.

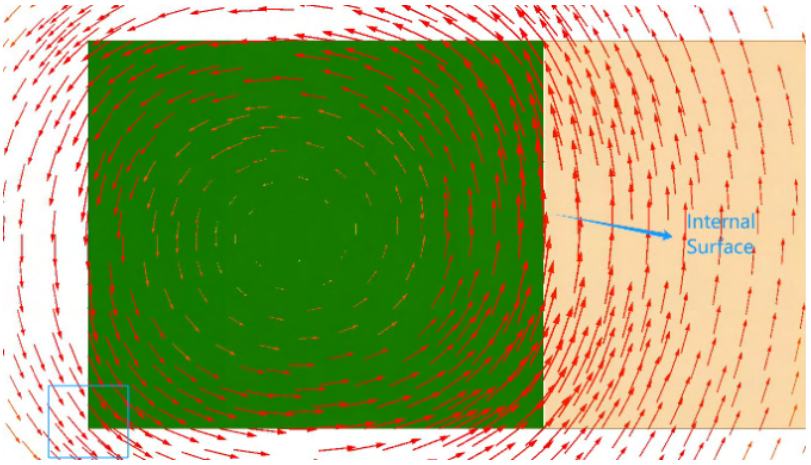

Figure 4.16: Magnetic Field within the winding pack (green region).

Figure 4.17 shows the variation of the critical current I_c with magnetic field strength at a field angle of approximately 50˚. A fitted expression for I_c from the figure is displayed in equation (4.5). Based on Figure 4.14 and equation (4.5), the critical current of the 4 mm wide HTS tape in the CREW HaT coils is around 80A at 10T and 40K.

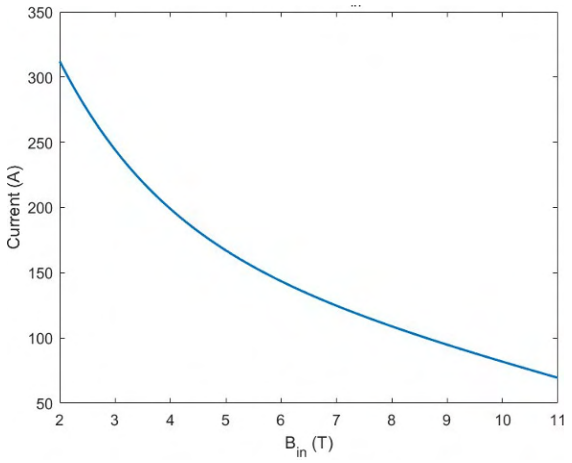

Figure 4.17: Critical current vs Magnetic Field with field angle of 50˚.

$$I_c = 391.65 \cdot e^{\left(-\frac{B}{1.96}\right)} + 3544736.36 \cdot e^{\left(-\frac{B}{310307.50}\right)} - 3544542.74 \qquad (4.5)$$

Other widths of the same YBCO tape will have different critical currents and applied magnetic field strength at a specific temperature. However, these scale linearly with the width of the tape.

4.6 Coil Conductor Options

Two common winding methods are used for wounding HTS coils using the YBCO tape conductor. As shown in Figure 4.18, the coils are wound using either a pancake or a layer wound configuration. In each case, one must consider that because the commercially available superconducting tape comes in limited lengths, joints may be necessary to connect conductor pieces in the winding pack to generate the coil's full required current or associated field strength. In the present case, a current of $1 \cdot 10^7$ amperes crossing through a section of the winding pack is required. As a reference, the maximum lengths of commercially available sections are 900 m for the simple tape from Superpower and 800 m for the cabled-tape configuration provided by the Advanced Conductor Technology Company.

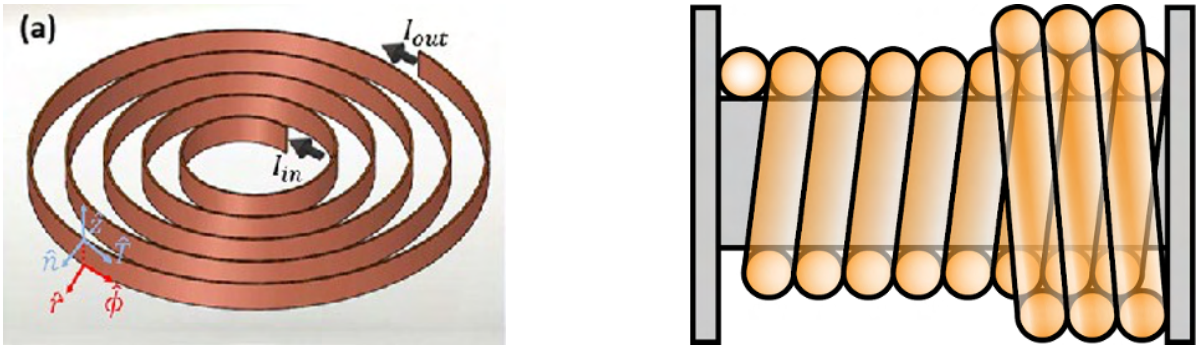

(a) Pancake wound (b) Layer wound

Figure 4.18: Conductors winding methods.

Due to the large size of the CREW HaT's coils, the distance around each turn is significant, resulting in a limited number of turns (< 50) being possible between conductor joints. Furthermore, as Figure 4.19 shows, the sample joints used to connect the YBCO tape are much larger than those of the single tape. Locating the joints on the inner or outer ends of a layer wound coil provides a convenient method for maintaining a compact winding pack. Therefore, a layer-wound configuration with joints positioned on the outer turns of each layer is chosen in the present design.

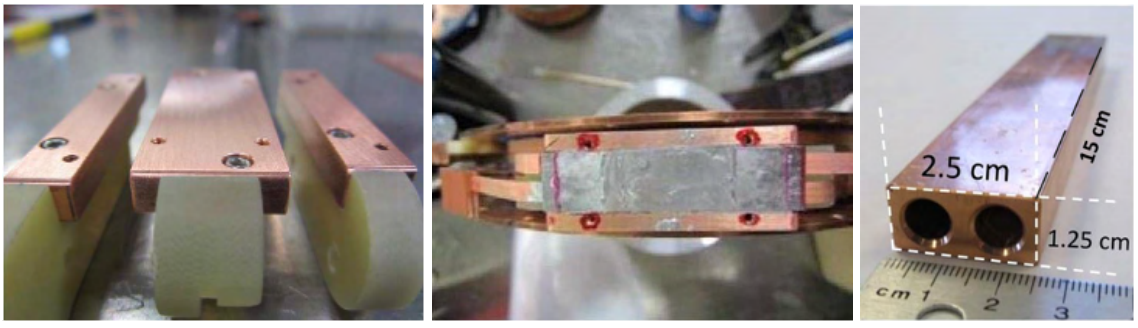

Figure 4.19: Examples of joint configurations for the YBCO tapes (left and middle) and the CORC conductor (right). Note the significant volume as compared to the tapes or conductors [40, 41].

4.6.1 Tape Option

SuperPower Inc. manufactures a 4 mm - 12 mm width YBCO tape that can be ideally used for winding coils in the Halbach array [38]. The crystal lattice structure of YBCO necessitates a tape-like geometry for the conductor, as outlined in Figure 4.20 [38]. The tape has an overall thickness of approximately 0.1 mm, and the thickness of each material comprising the YBCO-coated conductor is labeled in Table 4.2.

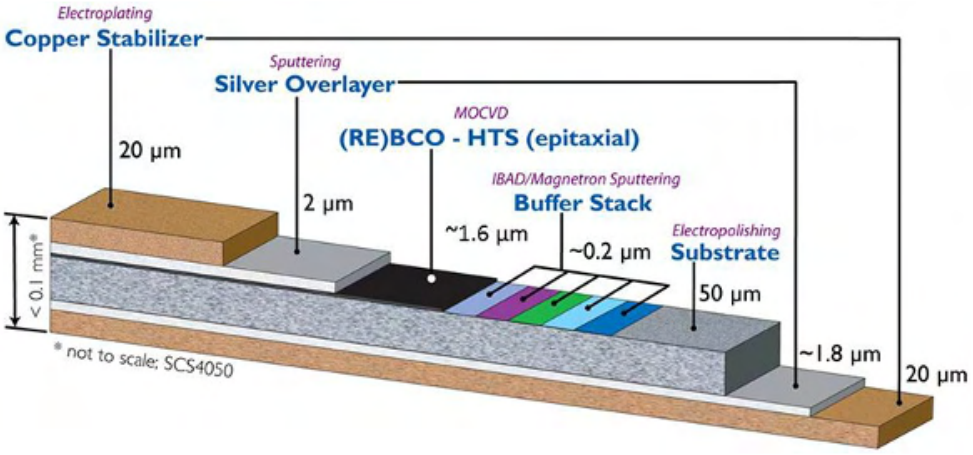

Figure 4.20: YBCO tape configuration for SuperPower 2G HTS wire [38].

Material	Layer Thickness
Copper stabilizer	40 μm
Silver overlayer	2 μm
YBCO	1 μm
Buffer stack	0.2 μm
Hastelloy C-276	50 μm
Silver overlayer	1.8 μm

Table 4.2: Material composition of the SuperPower YBCO coated conductor.

As estimated in Section 4.5, the critical current for 4 mm YBCO tape is around 80 amperes at 40 K and 10 T. Therefore, the number of turns needed to generate the total current of $1 \cdot 10^7$ amperes flowing through a section of the winding pack with the 4 mm tape is 125,000. Based on equation (4.8), the corresponding critical current of a 12 mm wide tape is around 240 A. Compared to using 4 mm tape, the number of turns of the 12 mm tape is reduced to 41,667. The winding pack geometry with the layer wound configuration is shown in Figure 4.21.

The layer number of the winding pack and thickness of the tapes are along the x-axis, and the turn number and width of the tapes are along the y-axis. In Figure 4.18, orange blocks are the YBCO superconducting tapes, black blocks are carbon fiber supporting the tapes, and gray blocks are joints used to connect each YBCO tape. The perimeter of the coil provides many possible locations for the joints, which can be offset from each other around the azimuthal direction.

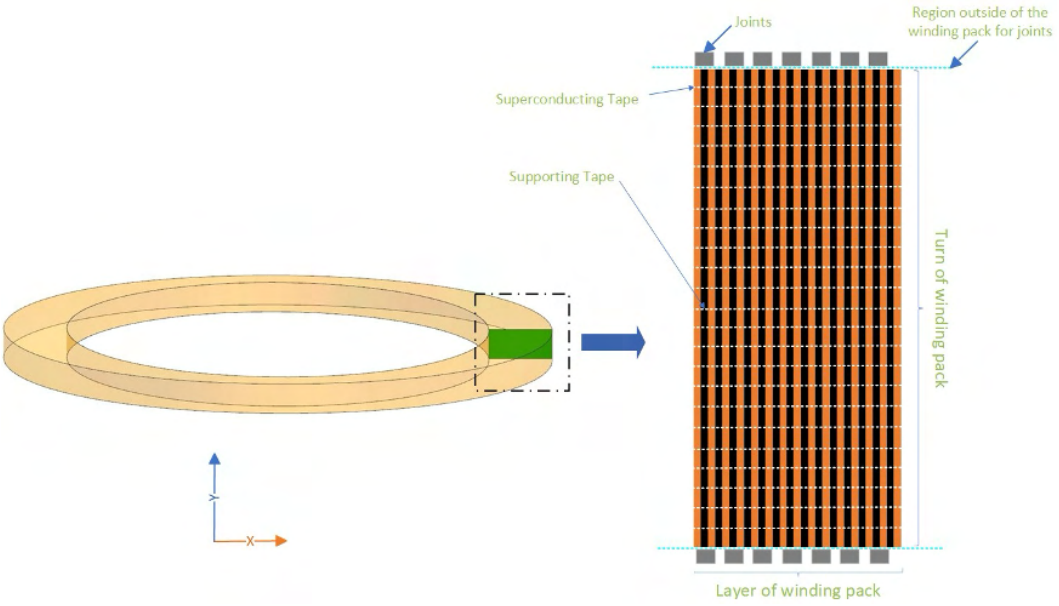

Figure 4.21: Winding pack configuration with the HTS tape option.

4.6.2 CORC Cable Option

The Conductor on Round Core Cabling (CORC) approach consists of the helical winding of superconducting tapes on a solid copper former [41]. Figure 4.22 shows the winding machine and the wound CORC cable.

Considering the tensile strain limits for different types of CORC cables, an 8 mm diameter CORC cable is chosen for the Halbach coils. The CORC cable comprises 48 pieces of 4 mm wide YBCO tapes on a 3.2 mm diameter of a solid copper former with a winding angle of 65°. The critical current of the selected CORC cable is about 3,800 A, and the required number of turns for the CORC cable is reduced to 2632.

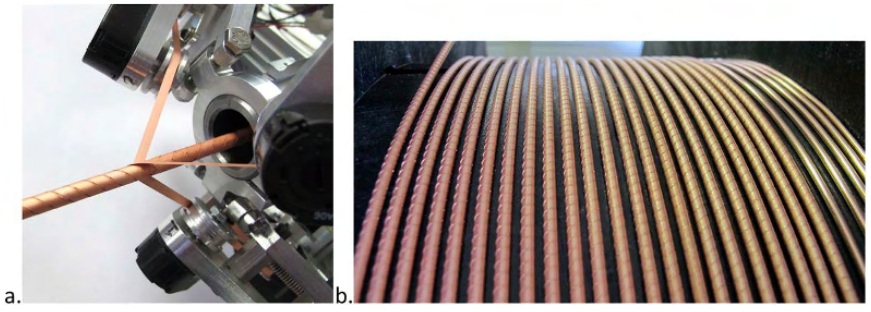

Figure 4.22: (a) Custom CORC® cable winding machine. (b) A 25 m long CORC® wire is being wound [40].

Equation (4.8) is used to determine the CORC cable's diameter, where *th* is the thickness of YBCO tape, which is 0.1 mm, and *i* is the layer number.

$$D_{CORC} = D_{core} + th \cdot i, \; i \in [1, N] \tag{4.6}$$

Similar to the tape winding pack geometry, the CORC coil winding geometry is shown in Figure 4.23. The layer number of the winding pack and thickness of the CORC cable are along the x-axis, while the turn number and width of the CORC cable are along the y-axis. The orange circles represent the CORC cables, the black regions comprise carbon-fiber supporting tapes, and the gray blocks are joints used to connect each length of the CORC cable.

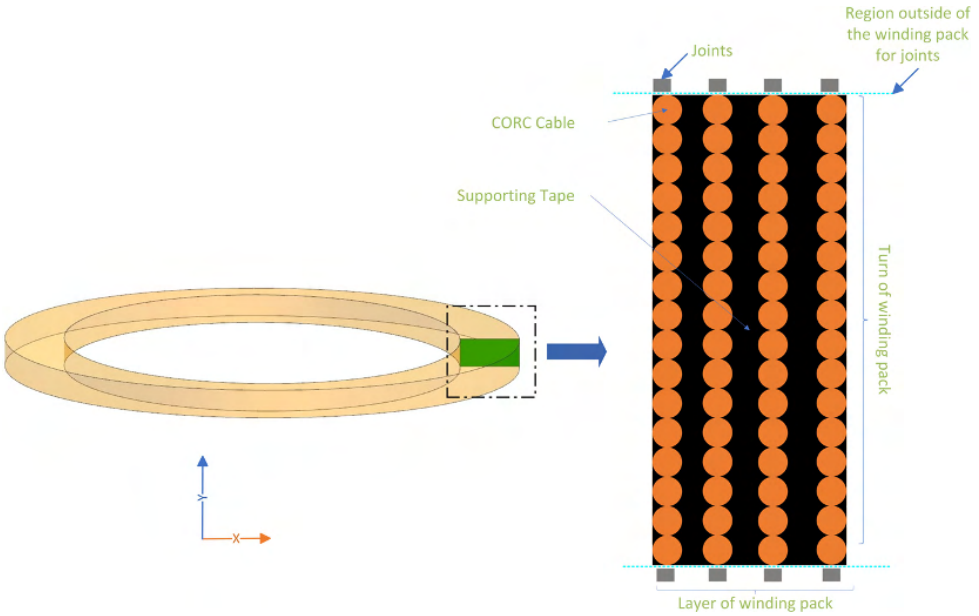

Figure 4.23: Winding pack of CORC cable option.

4.7 Number of Turns and Layers

Having determined the shape and dimensions of the coil, the necessary applied current, and the various options for the conductor elements, it becomes possible to calculate the number of turns and layers for the Halbach coils.

The number of turns is calculated based on the maximum available length of the conductor and the perimeter of each layer in the winding pack. For the elliptical coil, the perimeter is determined according to

$$p_i \approx \pi\left[3\left(a_i + b_i\right) - \sqrt{\left(3a_i + b_i\right)\left(a_i + 3b_i\right)}\right], \; i \in [1, N] \tag{4.7}$$

Here $a_i = R_{major}$ and $b_i = R_{minor}$ for each layer in the elliptical coil. The corresponding values of a_i and b_i are calculated as shown in equation 4.8. Based on the wire option, *th* can be either the YBCO tape's thickness or the CORC cable's diameter. $th_{supporting}$ is the thickness of

the supporting tape that is also dependent on the wire option and is explained in detail in the next section.

$$a_i = R_{major} + i \cdot \left(th + th_{supporting}\right)$$
$$b_i = R_{minor} + i \cdot \left(th + th_{supporting}\right),\ i \in [1, N] \quad (4.8)$$

For circular coils, the perimeter is determined by equation 4.9, where R is the inside radius of the coils.

$$p_i = 2\pi r_i,\ i \in [1, N]$$
$$r_i = R + i \cdot \left(th + th_{supporting}\right),\ i \in [1, N-1] \quad (4.9)$$

Table 4.3 summarizes the calculation results for all wire options and coil shapes considered. The average number of turns per layer using the 12 mm wide YBCO tape for the tape coil option is 40, resulting in a required number of layers at 1042. Similarly, the average number of turns per layer for the 8 mm diameter CORC Cable coils is 40, resulting in a required number of layers at 67.

	Tape	**CORC**
Conductor tape thickness	0.1 mm	8 mm
Kevlar tape thickness	0.25 mm	4 mm
Carbon fiber tape thickness	0.15 mm	2.3 mm
Cooling channel thickness	1 mm	NA
Turn	40	40
Layer	1042	67
Winding pack radial thickness	1.3 m	0.7 m

Table 4.3: Summary of Coil Parameters.

4.8 Supporting Tape Design

The large currents and magnetic field strengths associated with HTS coils generate significant tensile stresses in their conductor windings due to the associated Lorentz forces. According to their material composition, YBCO tapes only tolerate tensile stress up to 700 MPa [42]. For comparison, calculating the hoop stress for the Halbach coils using equation 4.4, one finds much larger stress values are created by the Lorentz forces. The Lorentz force generated hoop stress varies with the location of the winding pack, as shown in Figure 4.24.

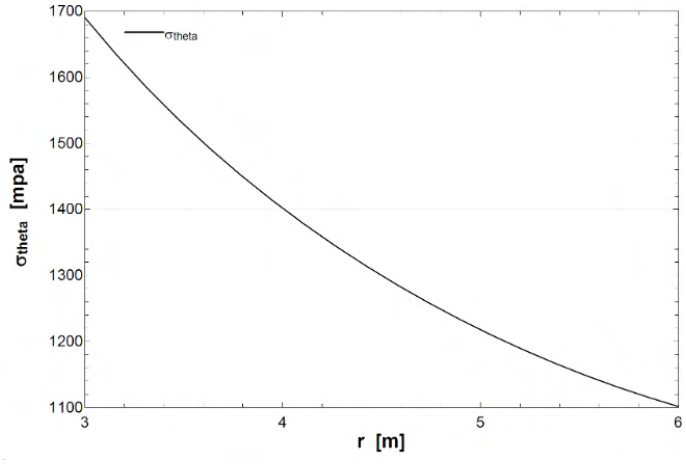

Figure 4.24: Hoop stress variation with location within the coil winding pack.

The corresponding average hoop stress is around 1400 *MPa*, and as induced on the HTS tape, greatly exceeds its yield strength. To remedy the problem, a layer of high-strength material will be co-wound with each turn of the tape conductor as depicted in Figure 4.25. Two materials satisfying the strength requirements are Kevlar and a Carbon-fiber reinforced composite.

Figure 4.25: Sketch of the supporting tape design.

Equation set (4.10) is used to calculate the thickness of the supporting tape to be combined with the different wire options. Here σ_θ is the average hoop stress calculated by equation (4.4), and σ_s is the tensile strength of supporting materials. A_c is the cross-section area of the conductor, and A_s is the cross-section area of the supporting tape.

$$\begin{aligned} F &= \sigma_\theta \cdot \left(A_c + A_s\right) \\ \sigma_s &= \frac{F}{A_s} \\ A_c &= w \cdot th_{YBCO} = \frac{\pi}{4} \cdot D_{CORC}^2 \\ A_s &= w \cdot th_s = \frac{\pi}{4} \cdot th_s^2 \end{aligned} \tag{4.10}$$

Table 4.3 summarizes the parameters of coils. Due to its higher tensile strength, the carbon fiber reinforced composite provides the best supporting material. The HEXCEL Company produces a high tensile strength HexTow IM Carbon fiber series, for which the tensile strength is over 6000 *MPa*, significantly higher than Kevlar's tensile strength of 3620 *MPa* [43]. The higher tensile strength results in additional advantages, such as a reduction of the thickness of the winding pack by about 40%, which in turn reduces the solar heat load and the mass of each Halbach coil by about 4%.

4.9 Stability and Protection

One of the most important considerations in designing superconducting coils is the conductor's thermal stability. If the local temperature of a superconductor rises above its critical temperature (this can be caused by a sudden tape motion under the influence of the Lorentz force or energetic particles hitting the conductor), this local "zone" loses its superconductivity and ohmic heating occurs. Such a region is called a "normal zone." If the normal zone is small enough, and heat transfer to its surroundings exceeds the volumetric heat generation within the normal zone, the normal zone will collapse [44]. However, if the normal zone exceeds a critical length and/or the heat generation exceeds the local cooling, it expands across the superconductor. The latter phenomenon is called "quenching."

When quenching occurs due to localized heating, it can damage the conductor and ultimately burn the coils. Therefore, it is important to detect a developing quench as early as possible using some form of quench detection. For larger magnets, shutting down the current supply is necessary. A suitable protection circuit can dissipate a high amount of stored energy through the protection circuit components, such as diodes, heaters, or resistors, rather than solely in the magnet winding. In some protection configurations, the stored energy can simply be dispersed more evenly throughout the volume of the coil, avoiding excessive localized temperature increases [45]. Further protection considerations are provided in the subsections below. The present section addresses stability issues for both tape and CORC conductor options.

4.9.1 Tape Wound Coil

The option of winding the coil with multiple turns of the single tape, either in the 4 mm or 12 mm width, presents the advantages of geometric simplicity and a straightforward method for incorporating the necessary structural supporting tape. However, the single-tape approach presents a significant risk. If at any point along the length of the nearly 1000 km of coil winding, and for whatever reason, a crack occurs across the width of the tape, the entire coil is rendered inoperative due to the arcing and heating that will occur at such a crack location. Furthermore, if the superconducting path through the YBCO layer is simply reduced rather than being interrupted so that the total current is larger than can be carried by the reduced superconducting cross-section, some local heating will occur, and sufficient cooling must be available to overcome the local heating, or the local temperature will rise.

For any temperature higher than the operating temperature T_{op} but lower than the critical temperature T_c, the critical current of the YBCO tape will drop, so the extra current (difference between I_{op} and I_c) will go through the copper stabilizer in the YBCO tape and generate heat (see Figure 4.26). This is called current sharing. For low-temperature superconductors, such a scenario typically results in a rapid growth of the normal zone, in part because the heat capacity of materials is so small at the typically low temperatures. For high-temperature superconductors such as the YBCO tape operating at 40 K, the heat capacity of the conductor is significantly larger, resulting in a low normal zone propagation velocity. A localized hot spot will be generated if or when a normal zone occurs in an HTS conductor (see Figure 4.27).

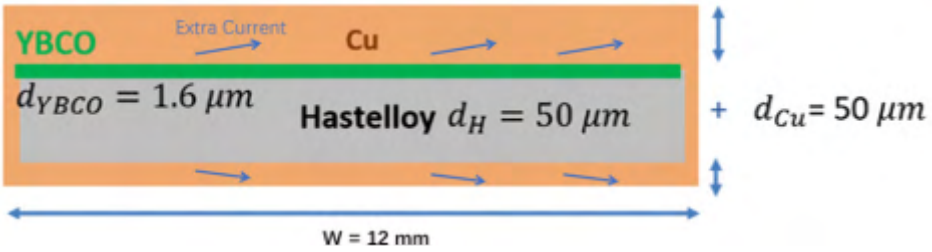

Figure 4.26: Current sharing in a simplified cross-sectional view of the YBCO tape conductor.

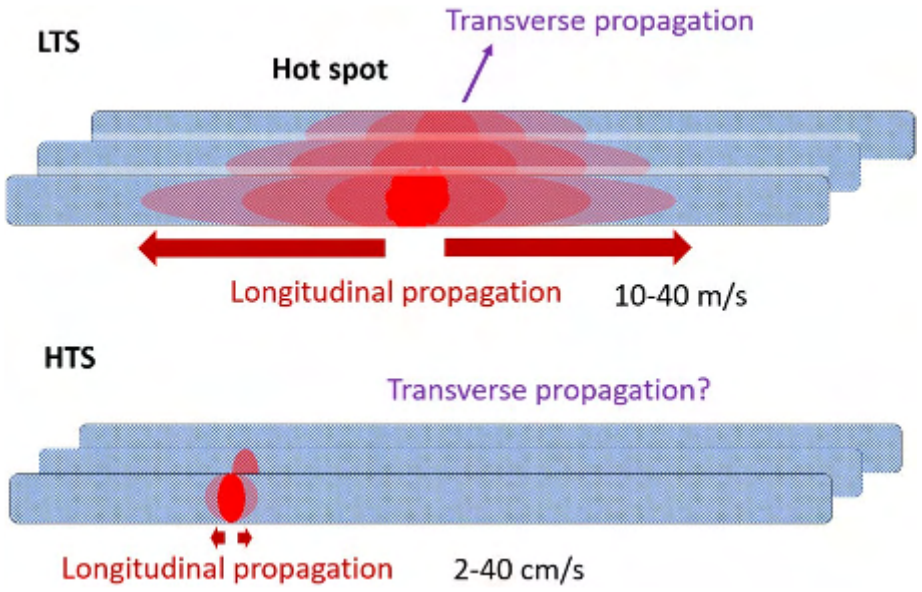

Figure 4.27: A sketch comparing normal zone propagation specifics in LTS and HTS coils [45].

To accommodate the possibility of any normal zones developing within the YBCO tape-wound coil, two different designs have been considered, each providing a cooling mechanism to counteract a possible normal zone occurring anywhere in the coil winding. Such an approach is reasonable for HTS tapes due to their more gradual transition to the normal state compared with LTS conductors. Each cooling option is incorporated using a layer-by-layer configuration to minimize the distance between any hot spot and the cooling

mechanism. The approach also results from considering the thermal resistance through each winding layer's various components. As shown in Figure 4.28 and Figure 4.29, any heat generated in the superconducting layer must flow through the adjacent layers of copper (surrounding the YBCO), Hastelloy, and structural support tape before reaching the cooling component. Noting the significant thermal resistance values shown in Table 4.4, one can conclude that each YBCO layer needs one cooling channel.

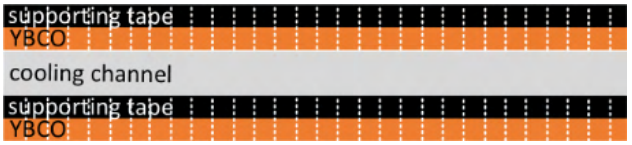

Figure 4.28: Cooling tape design.

Figure 4.29: Resistance network of the coils.

Component	Thermal Resistance
Copper	0.2064 K/mW
Hastelloy C-276	12.15 K/mW
Supporting tape	973.2 K/mW
Cooling channel	0.041 K/mW

Table 4.4: Thermal resistance of coil components.

4.9.1.1 AL Tape “Cooling Channel”

In the first cooling approach, a layer of RRR300 Aluminum (AL RRR300) is applied after each winding layer to form a “cooling channel.” AL RRR300 is used in this case because of its high thermal conductivity (> 1000 W/m-K) in the 40K – 60K range. Figure 4.30 shows the cooling channel design and analysis approach. Assumptions include an L = 5 cm long normal zone occurring in the center of the layer width, a 40 K boundary condition at the edges of the layer established by the coil’s refrigeration system, and an initial temperature of 100 K at the normal zone. Equation (4.11) is used to calculate the temperature-dependent heat flux generated by the normal zone, and equation (4.12) connects the heat generated by the normal zone with its evolving temperature and thermal conduction within the AL RRR300 layer. The

term ρ_e $(\Omega - m)$ represents the temperature-dependent electrical resistivity of the components in the YBCO tape.

$$Q_g = I^2 \cdot \rho_e(T) \cdot \frac{L}{w \cdot th} \tag{4.11}$$

$$\frac{Q_g}{2} = \frac{P \cdot th_c}{L/2} \cdot \int_{40K}^{T} k(T)dT \tag{4.12}$$

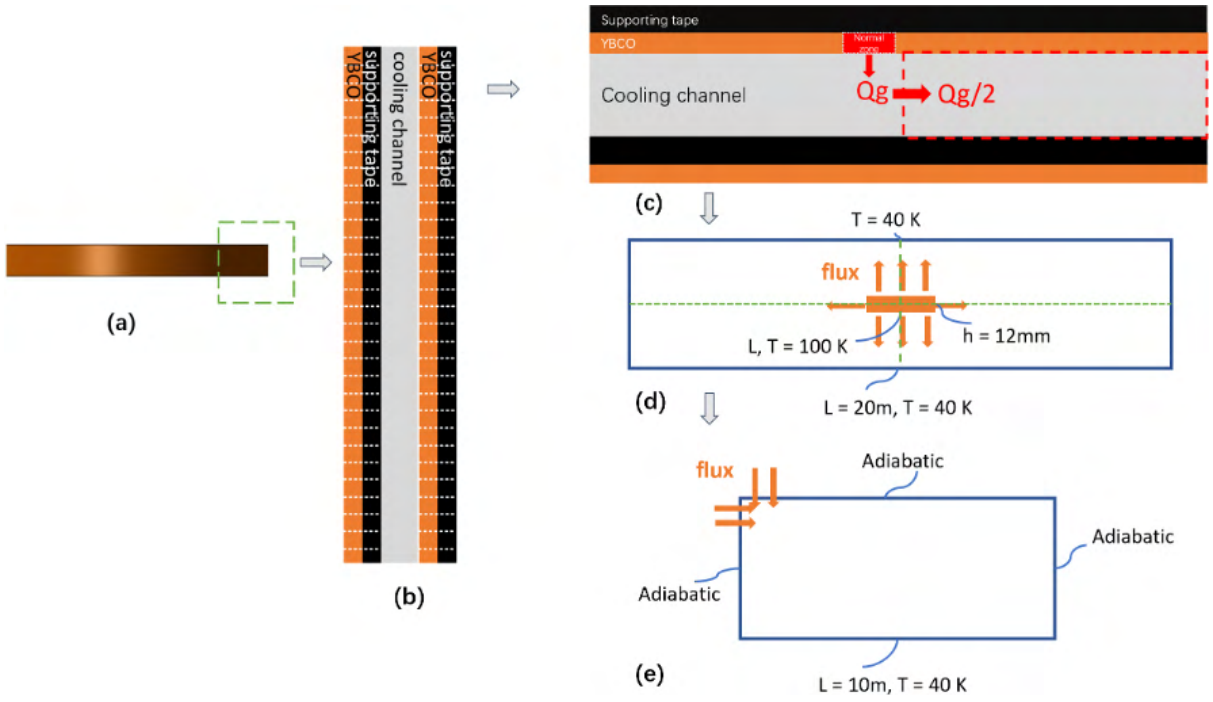

Figure 4.30: Cooling tape design sketch. (a) section of the Halbach coil, (b) winding detail showing multiple turns of the YBCO tape and structural support tape as well as the layer-wide AL RRR300 'cooling channel', (c) depiction of a local hot spot in the YBCO, (d) heat flow from hot spot out through the cooling channel, (e) thermally symmetric section of the cooling channel used for the numeric analysis of resulting temperature profile.

Figure 4.31 presents the steady-state results obtained from the thermal model available within Solidworks [46] when the thickness of the cooling tape is 1 mm. The high temperatures (near 650 K) developed at the hot spot location suggest that either a thicker layer of AL RRR300 or an alternate approach is required.

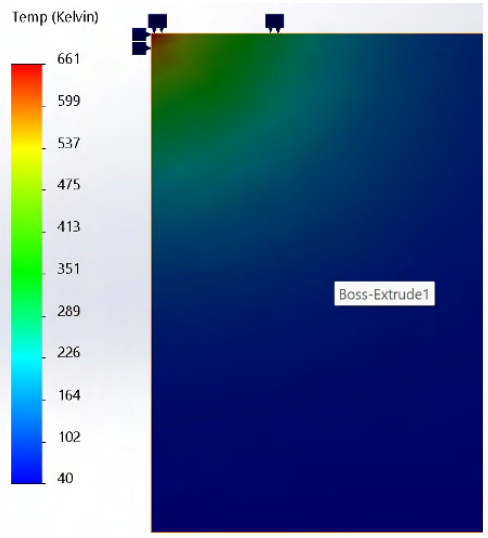

Figure 4.31: Temperature distribution in 1 mm thickness of cooling tape.

4.9.1.2 Helium Flow Cooling Channel

The second cooling channel approach, utilizing a flow of cold helium gas, is shown in Figure 4.32. Here, a separate channel is also envisioned for each winding layer. Like the solid aluminum channel, it extends across the full width of a winding layer and occupies a radial thickness of 1 mm. The helium flow enters the channel at one azimuthal location on one end of the layer width and exits near the same azimuthal angle, making a full turn around the coil but at the other end of the layer width. Figure 4.32b shows the structure of the channel. The wall thickness of the square channel is 0.25 mm.

Assuming the same normal zone and heat generation as in the AL RRR300 example above, the performance of the helium cooling channel with an assumed mass flow rate of 0.88 g/s results in a tolerable temperature rise of only 16 K at the hot spot location. Table 4.5 summarizes the parameters of the helium flow channel, where ΔT is defined as

$$Q_g = c_p(T, P) \cdot m_{dot} \cdot \Delta T \tag{4.13}$$

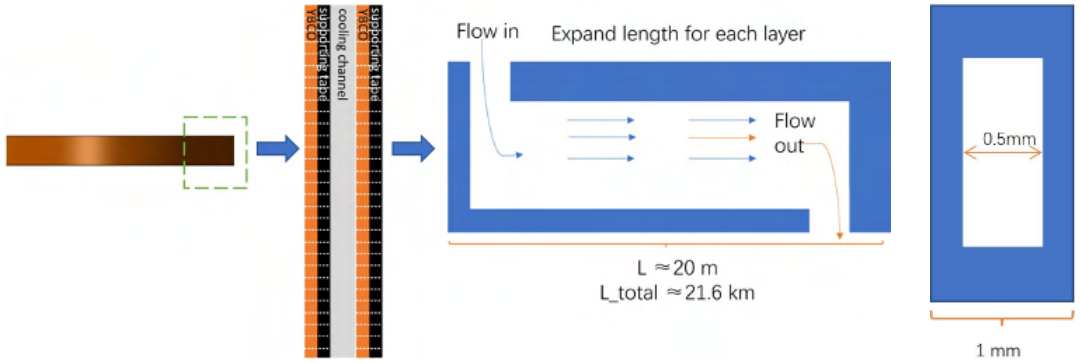

(a) Expand view (b) Side view

Figure 4.32: Helium flow cooling channel design.

Helium Gas Flow Parameters	
v	0.2 m/s
m_{dot}	0.88 g/s
Re	699
P_{in}	20 bar
ΔP	8.2 bar
ΔT	16 K

Table 4.5: Parameters of the helium flow channel.

4.9.2 CORC Cable Wound Coil

In contrast with the tape-based coils, coils wound using the CORC do not present the same stability challenge, do not need the extra cooling channel design, and are inherently safer than the tape-based coils.

As described in Section 4.6.2, the CORC cable is composed of YBCO tapes wound helically in layers around a solid copper former core (See Figure 4.33). By operating at a suitable margin below the cable's full capacity, normal zones can be avoided even if one of the tapes in the cable is broken across its full width. In such a case, the remaining tapes share the extra current and continue to conduct at a slightly higher current without generating any heat. Furthermore, if a normal zone does develop in one of the tapes, the heat generated can be removed through the copper stabilizers of multiple superconducting tapes and the solid copper former core. Therefore, there is no significant change in temperature or generation of a heat spot in the CORC cable. Coils wound from single tapes, carrying no more than a few hundred Amperes of current, resulting in a relatively high magnet inductance that creates a risk of localized burnout [41]. The CORC cable can easily carry over thousands of amperes of current and still can be safely operated even if a few wires are broken.

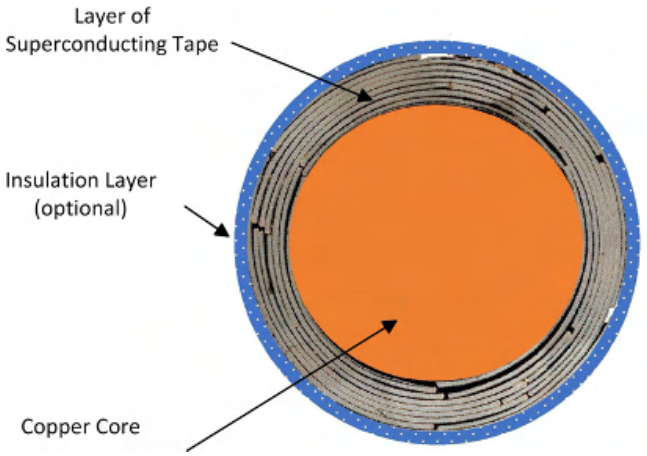

Figure 4.33: Cross-area section of CORC Cable.

Safety is paramount for space travel, and CORC cables are more reliable in terms of safety. At the same time, the CORC-based coils have a smaller surface area and self-induction (see Tables 4.3 and 4.6), thus absorbing less solar flux and requiring a shorter charge or discharge time in space. For all these reasons, the CORC wound coil option is preferred for the CREW HaT design.

4.9.3 Coil Protection

Although HTS equipment is stable when subjected to certain disturbances, it is important to have a protection design for HTS equipment since it is often an expensive component of the system [47]. Key areas for protection include:

1. Overheating (hot spots), as discussed in Section 4.9.1.
2. Arcing (high-internal voltages), to be considered in future work.
3. Overstressing (fault-mode induced excess current in a coil or coils within a nested-coil magnet or as induced by differential thermal expansions) is to be considered in future work.

Figure 4.34 illustrates the two types of thermal runaway issues for HTS magnets. The first case is a natural thermal runaway that emerges above the coil's critical current. The natural thermal runaway is usually predictable and can be avoided if the operating current is below the critical current of the coils. However, it is unpredictable when an HTS coil is inductively coupled with other surrounding coils [48]. The second case is a premature thermal runaway emerging below the coil critical current. It is also unpredictable and harmful for the REBCO magnet as a sudden voltage increase [48].

Equation (4.15) defines the stored energy in coils, where L is the self-inductance of the single coil and is defined by Equation (4.16). P_0 is the constant and is defined as

$$P_o = 4\pi \cdot \left[0.5 \cdot \left(1 + \frac{z^2}{6}\right) \cdot ln\left(\frac{8}{z^2}\right) - 0.84834 + 0.2041 \cdot z^2\right] \tag{4.14}$$

The term $z = \frac{c}{2a}$ where a is the mean radius of the coils, c is the thickness of the coils, and N is the number of turns in the coil. Table 4.6 shows the stored energy and self-inductance of different wire option coils.

$$E_m = \frac{LI^2}{2} \tag{4.15}$$

$$L = 0.001 \cdot a \cdot N^2 \cdot P_o \cdot 10^{-6} \tag{4.16}$$

	Tape	CORC
Stored Energy (MJ)	4.43	4.59
Self-Inductance (Henry)	153.9	0.64

Table 4.6: Stored energy and self-inductance of coils.

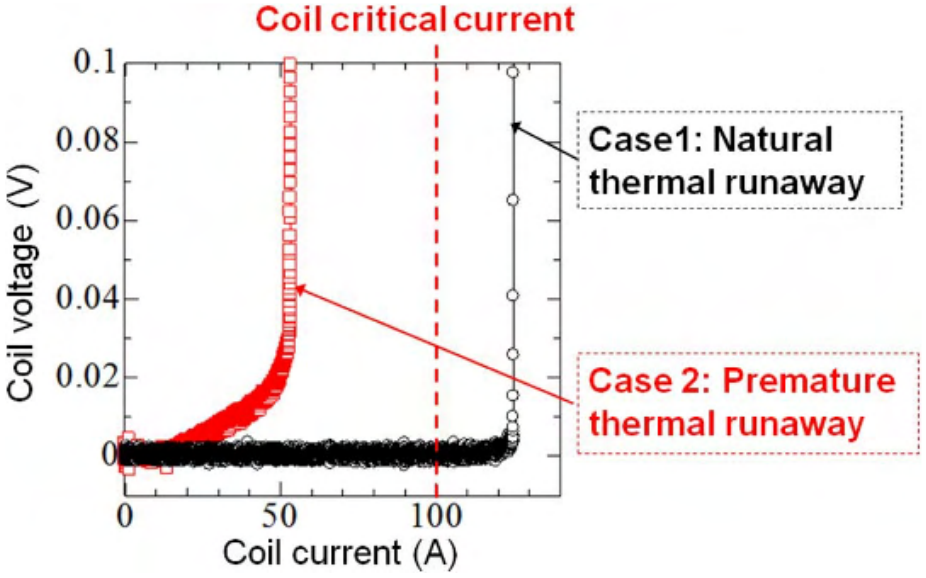

Figure 4.34: Two types of thermal runaway for HTS magnets [48].

As the coils' stored energy reaches the MJ level, quench detection, protection, and energy extraction are normally put in place to prevent the quenching conductor from experiencing thermal damage [45].

The magnetic method for quench detection works as a Hall sensor and was used to detect the current distribution in the space between current-carrying ReBCO conductors [45]. The main advantage of monitoring the redistribution of current rather than the appearance of resistive voltage is that this method is much more sensitive [45]. Recently, this technique has been applied successfully in a ReBCO-based CORC cable [49] (see Figure 4.35).

Future work will consider protection circuits and energy extraction design more extensively.

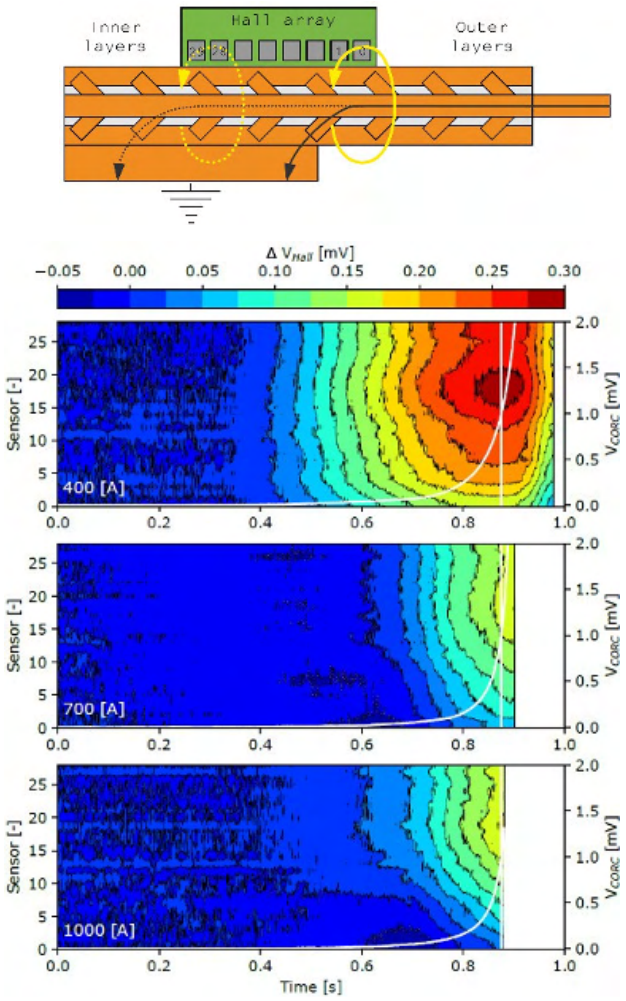

Figure 4.35: A practical implementation of the same technique in the form of a hall array embedded in the current terminals of the CORC cable [49].

4.10 Mass of Coils

Mass is one of the important considerations for transport into space. The design of the coils needs to be as light as possible and must consider the rocket's carrying capacity and energy consumption ratio. As discussed in Sections 4.3 and 4.4 above, two shapes of coils and conductor options are being considered. In addition, two different wire arrangements are possible, as shown in Figure 4.36.

When winding the conductor, the thickness of the coil gradually increases with each layer, and the length of the conductor used for winding each layer also gradually increases, especially if the number of turns per layer is fixed. Because of the conductor length limitation, the maximum number of turns used to wind the coil is constrained by the number of turns for the outside layer in the coil. Maintaining the same number of turns for all the other layers guarantees that the winding length of the conductor in each layer is under the length limitation. Such a winding choice is called a fixed turns arrangement and is shown in Figure 4.36a.

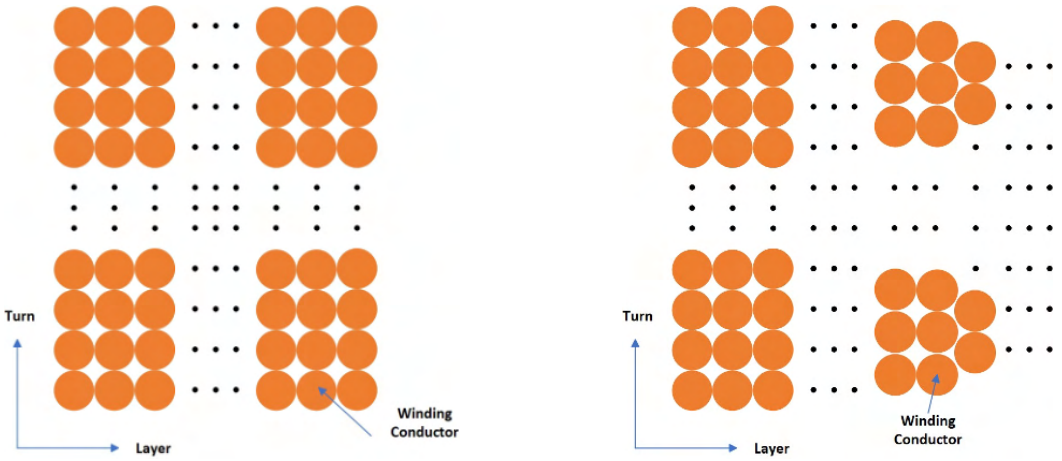

(a) Fixed turns arrangement (b) Non-fixed turns arrangement

Figure 4.36: Coil winding arrangements.

Alternatively, if one attempts to wind the conductor as long as possible in each layer, the number of turns will vary with the layer number and will depend on the maximum length of the conductor. As the thickness of the winding pack gradually increases, the length of the conductor used for winding each layer increases until the length limit is reached. To ensure that the conductor length does not exceed the length limit, the number of turns must decrease to avoid exceeding the maximum length. Such a winding choice is called the non-fixed turns arrangement and is shown in Figure 4.33b. Each situation was coded in MATLAB to determine the associated mass. Finally, the best choice is the circular CORC coil winding with the non-fixed turns arrangement, and the mass of a single coil is 15.5 tons.

4.10.1 Tape Wound Coil

As mentioned in Sections 4.6, 4.8, and 4.9, the tape wire option coil includes three components: the YBCO tapes, the supporting tapes, and the cooling channels, and the maximum length of YBCO tape is 900 m. The elliptical coil used for the mass calculation has an average semi-major radius of 4 m and an average semi-minor radius of 2 m. Similarly, the circular coil used to do the mass calculation has an average radius of 3 m. The mass of each component is shown in Figure 4.37. Figure 4.37a shows the mass of each component in an elliptical coil with the fixed turn arrangement. Because of the fixed turn number, the length of YBCO in each layer increases linearly, as do the masses of each component. When using the non-fixed turn arrangement, the length of YBCO will increase until it reaches the length limitation. Then, reducing the number of turns by one each time the winding length reaches the limit enables one to continue the winding to the final layer. The mass of each component in the non-fixed turn arrangement appears as a saw-tooth function, as shown in Figures 4.37b and 4.37c.

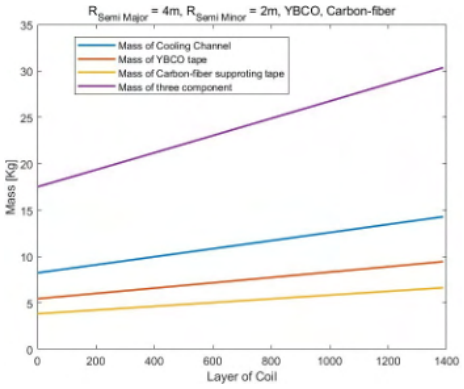

(a) Mass of each component in an elliptical coil with fixed turn arrangement

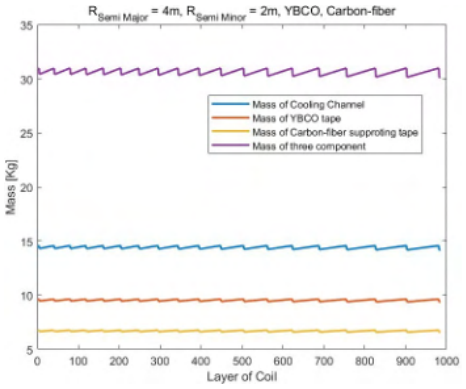

(b) Mass of each component in an elliptical coil with non-fixed turn arrangement

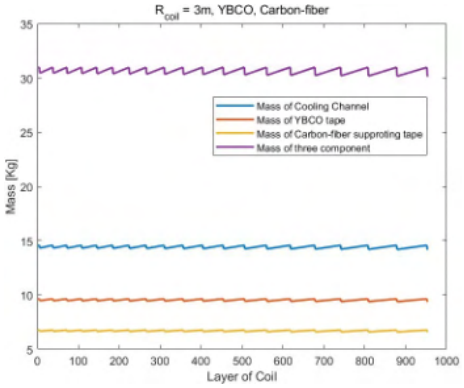

(c) Mass of each component in a circular coil with non-fixed turn arrangement

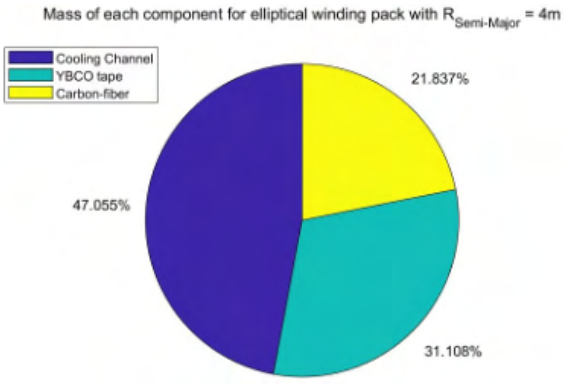

(d) Mass ratio of each component

Figure 4.37: Mass of each component in tape-wound coils.

By comparing Figure 4.37a and 4.37b, one finds that the total conductor length for the non-fixed turn arrangement is much less than with the fixed turn arrangement for the same coil shape.

A few additional benefits of reducing the total conductor volume may also be noted. First, it reduces the thickness of the winding pack. When calculating the solar flux in Section 4.11, a reduced winding pack thickness will also reduce the surface area and the corresponding absorbed solar flux. Second, the mass can be reduced. By calculation, the mass of the coil with the non-fixed turn arrangement can be reduced by 10% compared with the fixed turn arrangement. Thirdly, fewer layers means fewer connecting joints, which proportionally reduces the joint-generated heat. Furthermore, by using the non-fixed turn arrangement, the length of YBCO in each layer is roughly the same. This means the YBCO lengths do not need to be individually customized, reducing material waste and cost.

Comparing Figure 4.37c and 4.37b, one finds that the number of winding layers required for the circular coil is less than that required for the elliptical coil. In other words, the benefits from the circular shape coil are more pronounced than those of the elliptical coils. The results of tape-wound coils with the non-fixed turn arrangement are shown in Table 4.7. Not

surprisingly, the tape wire option coils are very thick and heavy, and about half of the weight is the cooling channel, as shown in Figure 4.37. Furthermore, designing such a long cooling channel is also a big challenge. Therefore, the tape-wound coil is not a good choice for this project.

	Elliptical Coil	Circular Coil
Average number of turns	42	43
Layers	985	954
Radial thickness of winding pack (m)	1.43	1.38
Mass (ton)	30.2	29.2

Table 4.7: Results table of tape wire optional coils.

4.10.2 CORC Wound Coil

The mass optimization process has also been carried out for the CORC wound coils. As discussed in Section 4.6.2, the CORC winding has three main components: the copper core, the YBCO tape, and the supporting tape. Through optimization, the lightest weight achieved is around 15.2 tons for circular coils with the non-fixed turn arrangement. Due to the similarity of the mass figures, only the mass of the circular coils with non-fixed turn arrangement is shown (see Figure 4.38). The majority of the mass (66%) is contributed by the YBCO tape, as shown in Figure 4.38b.

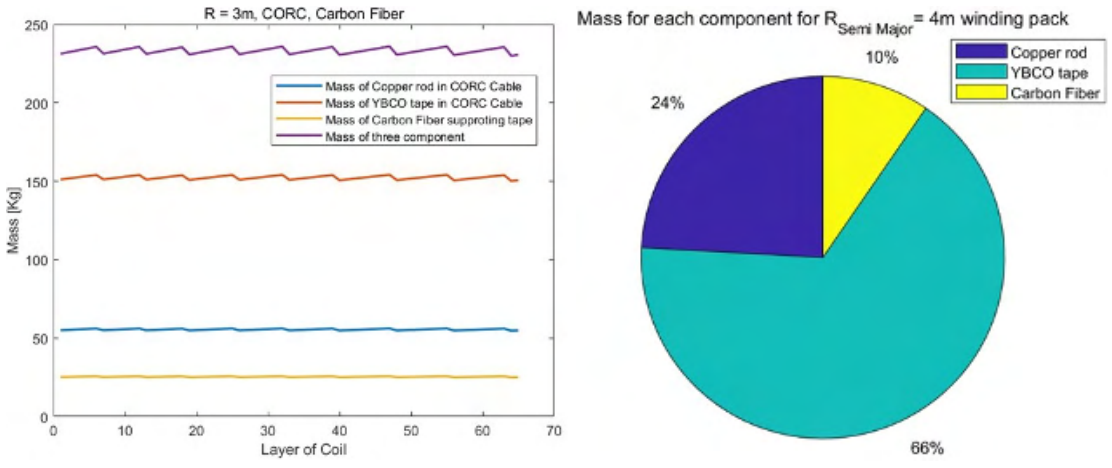

(a) Mass of each component in a circular coil with unfixed turn arrangement

(b) Mass ratio of each component

Figure 4.38: Mass of each component in CORC wire option coils.

The length of the CORC conductor used to wind the coils is limited by the maximum length of YBCO tape used in co-winding the cable, which is 900 *m*. The corresponding maximum length of CORC that can be manufactured is 800 *m*. The length of YBCO is determined according to equation 4.17, where P_i is obtained from equation (4.7), while Pt and Cs are shown in Figure 4.39.

$$L_{YBCO} = \frac{P_i}{P_t} \cdot C_s \tag{4.17}$$

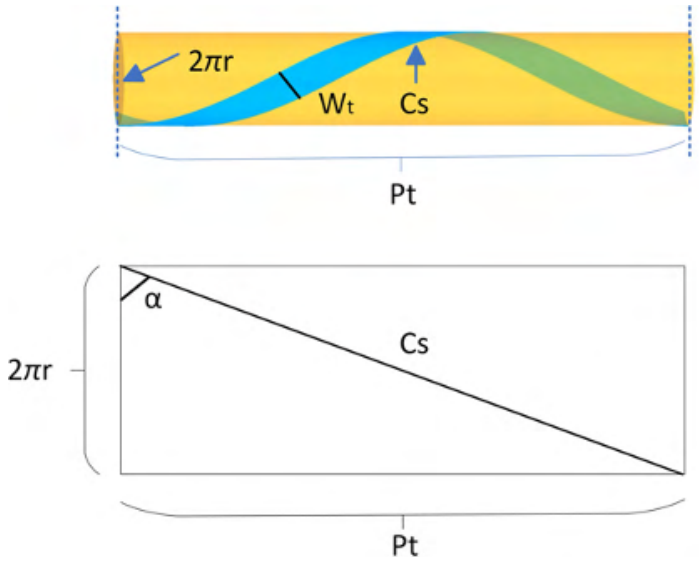

Figure 4.39: Calculation of length of YBCO tape used in CORC Cable

Table 4.8 summarizes the calculations showing that the circular coils are 3% lighter than the elliptical ones. By comparing Table 4.7 and 4.8, the CORC wound coils are much better than the tape wound coils because both the mass and thickness of the winding pack are reduced by 50%.

At present, the core used in the CORC cable is copper. If replaced by aluminum, the mass of a single circular-shaped coil can be reduced to 12.6 tons, which represents a 17% reduction. However, replacing the copper core with an aluminum core may cause thermal issues and other complications. Further research on this option needs to be conducted in Phase II.

	Elliptical Coils	Circular Coils
Average turns / layer	40	41
Number of Layers	67	64
Radial thickness of the winding pack (m)	0.67	0.64
Mass (ton)	15.6	15.2

Table 4.8: Results table of CORC wound coils

4.11 Cryogenics

The working temperature of the Halbach array system, 40 K, requires special cryocoolers with robust cooling power. The following section will investigate the most important aspects of heat sources in this research project and the potential choice of cryocoolers.

This project's three main heat sources are solar flux absorbed by the coils, resistive heat generated by the joints, and heat conducted and generated along the current leads from the high-temperature power source to the cryogenic coils. In descending order, for the CORC wound coils, there are 135 W of resistive heat generated from the joints, 40 W of solar flux, and 10 W from the current leads. The tape wound coils have 50 W of solar flux, 28.81 W of resistive heat generation, and negligible heat load from the current leads.

Three types of cryocoolers are identified as viable cooling options based on the total heat load. These are (a) Reverse Brayton Cycle Cooler, (b) Looped Thermo-acoustic Cooler, and (c) Hybrid Stirling / Pumped Helium Cooler. Each option has disadvantages and advantages, and further research and development are required before making a final selection.

4.11.1 Heat Load

The CREW HaT system will operate in space, and because space is a vacuum, radiation is the only form of heat transfer. The primary source of heat is the sun, with a surface temperature of 5780 K and about 1.5×10^8 km away from the spacecraft [50]. The second heat source comes from the resistive heat generated at the joints between each layer in the superconducting coils. The third source is associated with the current lead transferring electric (and thermal) energy from the solar panels to the superconducting coils.

4.11.1.1 Solar Flux

In determining the solar radiation heat load on the Halbach array, multiple conservative assumptions are included. The first is related to the orientation of the array with respect to the sun. As shown in Figure 4.45, the maximum incident solar flux occurs when five of the coil surfaces face the sun. Here, the entire cross-sectional area of coil 1 and coil 5 receive the incident flux while that received by coils 2 – 4 is a projected area.

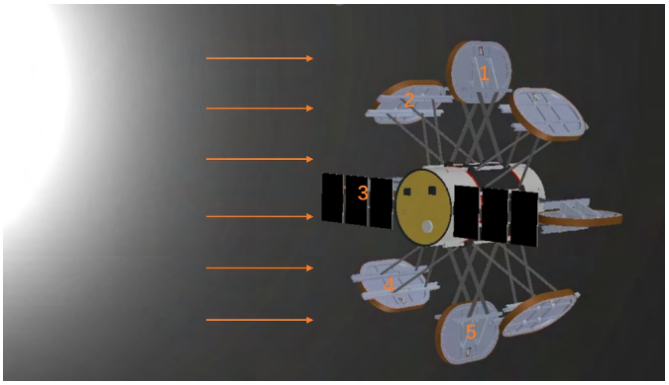

Figure 4.40: Solar flux incident on the CREW HaT system. Figure from [35].

Equation 4.18 relates the heat transfer from the sun to the coil. Here, σ is the Stefan-Boltzmann constant, ε is the effective emissivity of the surface, $F_{sun,coil}$ is the view factor from the sun to the coil, A_{sun} is the surface area of the sun, T_{sun} is the surface temperature of the sun, T_{coil} is the surface temperature of the coil, and A^* is the area of coils shown in table 4.9. Multi-layer insulation (MLI) is used to cover the coils and to reduce the absorbed radiation at their surface. For single-layer insulation, the typical value of ε is around 0.03, while for multi-layer systems, the value of q scales as 1/(N+1), where N is the number of layers. Assuming an 80-layer MLI blanket, one can represent the emissivity as a value of $\varepsilon/(N+1) = 3.7\,x\,10^{-4}$. Using $\varepsilon = 3.7 \times 10^{-4}$, Equation 4.18a yields 40 W of solar flux for CORC wound coils and 50 W for tape wound coils, as summarized in Table 4.9.

$$q_{coil} = \sigma\varepsilon A_{sun} F_{sun,coil}\left(T_{sun}^4 - T_{coil}^4\right) \tag{4.18a}$$

$$F_{sun,coil} = \frac{A^*}{A_{orbit}} \tag{4.18b}$$

	CORC wound coils	Tape wound coils
$A_{1,5}^* (m^2)$	22.65	27.1
$A_{2,4}^* (m^2)$	16.02	19.16
$A_3^* (m^2)$	1.39	2.16
$q_{coil,total}$ (W) for 8 coils	39.65	47.67

Table 4.9: Solar flux summary of coils.

4.11.1.2 Resistive Heat Flux

The heat flux generated from the resistive joints in the superconducting coil represents a second significant source of heat generation for the Halbach array. The joint resistances for

the coils are all in series, and the resistive heat flux of the coil can be described by Equation 4.19. Table 4.10 summarizes the results of the resistive heat flux for the eight coils. For the CORC wound coils, each joint's resistance is $1.82 \times 10^{-8}\ \Omega$ [51], generating 17.6 watts for each coil and a total of 140.9 W of resistive heat flux for the 8 coils. For tape wound coils, the joint resistance is $6 \times 10^{-8}\ \Omega$ [35], generating a total of 28.81 watts of resistive heat flux for the 8 coils.

$$q_{joints} = I^2 R_{joint} N_{joint} \tag{4.19}$$

	CORC wound coils	Tape wound coils
Applied current (A)	3800	240
$R_{joint}(\Omega)$	$1.82\ x\ 10^{-8}$	$6\ x\ 10^{-8}$
$N_{joint}/coil$	67	1042
$q_{joint}(W)$ for 8 coils	140.9	28.81

Table 4.10: Resistive heat flux summary of coils.

4.11.1.3 Current Leads

Current Leads represent the coils' third significant source of heat load. The leads carry electric and thermal energy from the power source (assumed at ~ 298 K) to the coils at 40 K via transmission wires. In terrestrial applications, the aspect ratio of a conduction-cooled current lead is optimized to minimize the sum of the heat conducted down the temperature gradient and the resistive heat generated along the lead. In the CREW HaT application, additional features must be included to account for radiative heat rejection along the current lead and the absence of heat generation in the superconducting portions of the lead. Figure 4.41 displays the key features of a 1-D model developed to determine the current lead's heat load at the coil end. The transition temperature T_t is set at 89 K, and the values associated with the geometry of the resistive section and the heat load at the coil-end of the current lead (T_c) are summarized in Table 4.11. In this model, the current lead extends between the room and superconducting coil temperatures for each of the 8 coils, and the resultant heat load displayed is the total for the 8 coils.

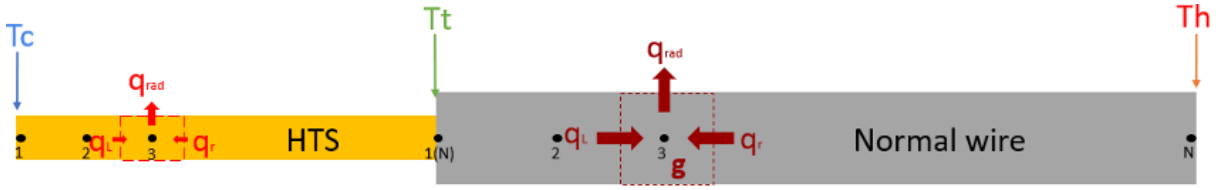

Figure 4.41: Current lead model features.

	CORC wound coils	Tape wound coils
$A_c(mm^2)$	9.69	0.48
$L(m)$	1	1
$q_{CL}(W)$	9.92	0.256

Table 4.11: Summary of current lead parameters.

Combining the three sources of heat load results in a total heat load to the CORC wound coils of 190.82 W and the tape wound coils of 76.5 W.

4.11.2 Cryocooler Options

A forced flow cooling system is envisioned for each of the 8 coils in the Halbach array. The cold gas originating from a cryocooler located on the spacecraft will flow out to channels traversing the perimeter of a coil on both of its axial ends and then return to the cryocooler for a closed-loop system. The primary goal of the flow path geometry is to bring the cold gas in direct contact with the conductor joints that will be located at the ends of each layer of the coil winding. Design parameters such as flow path configuration (parallel or series connected flow paths), mass flow rates, associated pressure drop, electric power consumption, and cooling power will all need to be addressed in phase II activities.

The following three sections briefly describe options for cryocoolers to provide the required cooling power. Each option is based on existing reports of cryocoolers that provide the appropriate order-of-magnitude cooling. However, in each case, significant development will be required to match the anticipated design requirements for the Halbach coils. The history of cryocooler development is one of continual progress, increased capacity, and improved efficiency. The push provided by our Phase II investigation will benefit both the Mars Mission and the overall cryocooler industry and applications such as quantum computing, other aerospace applications, and ground-based superconducting power applications.

4.11.2.1 Reverse Brayton Cycle Cooler

The Creare company of Hannover, New Hampshire [52], has a long history of successfully developing Reverse Brayton (RB) Cycle cryocoolers for aerospace applications. One of their coolers is presently operating on the Hubble Space Telescope. Recent conversations with Creare [28] indicate that a version of the cooler displayed in Figure 4.42 could provide 45 watts of cooling at 40 K. The neon working fluid, at a mass flow rate of 19.5 g/s, would draw an input power of 1.4 kW. The overall mass of the cooler is estimated at 80 kG.

Figure 4.42: Reverse Brayton Cycle Cooler.

Among the various issues that must be addressed for the RB cooler during a phase II investigation will be the operation of the turbo-alternator component within the magnetic field existing in the spacecraft. The RB cooler option provides the advantage of near-scale units at a mature development level. The large mass is a disadvantage.

4.11.2.2 Looped Thermoacoustic Cooler

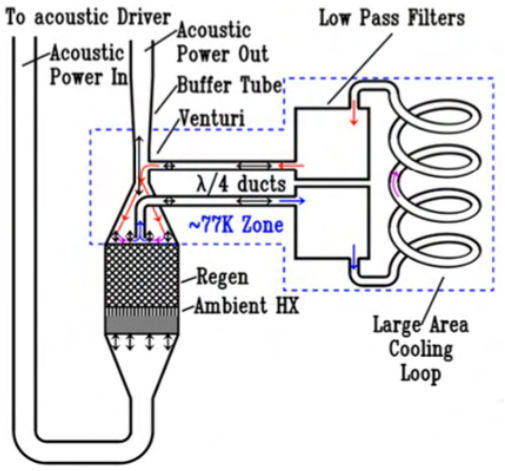

At the 2022 International Cryocooler Conference, Etalim, Inc. reported the concept of a Thermo-acoustic cooler utilizing a self-circulating loop [54]. The self-circulating flow loop takes advantage of the pressure drop associated with a venturi mechanism (see Figure 4.43) to convert the standard alternating flow of a thermo-acoustic driven system into a directed flow. Etalim, Inc. demonstrated the operation of the system in a thermo-acoustic waste heat recovery engine and projected that a large cooling power can be achieved by the high operating frequency (490 Hz) flexure-based cryocooler.

Figure 4.43: Looped thermoacoustic cooler.

They also noted that the system without any sliding components or valves enables a highly reliable compact machine with high specific power.

Projections based on prior performance predict that more than 50 W of cooling at 40 K would be possible with an input power of ~ 2 kW. The cooler would be charged to 8 MPa with helium gas and would utilize a diaphragm-driven acoustic power source operating at 490 Hz. The total mass of the cooler is estimated at 34 kg.

During a Phase II investigation, continued conversations with Etalim, Inc. will be required to revisit and confirm performance estimates. The Thermo-acoustic cooler presents the advantages of high reliability and low mass, with the disadvantages of significant development and performance demonstrations.

4.11.2.3 Hybrid Stirling / Pumped Helium Cooler

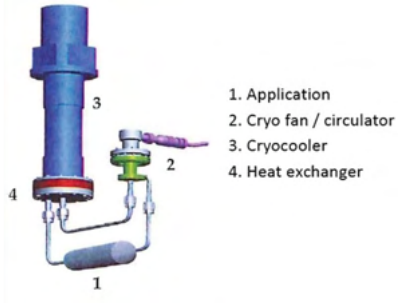

The third cryocooler option combines the cooling power of commercially existing Stirling cryocoolers with a secondary pumped flow circuit of helium gas (see Figure 4.44).

Figure 4.44: Hybrid Stirling / pumped helium cooler.

The hybrid cooler is under development at SHI Cryogenics [55], which reports performance demonstration down to 40 K with cooling power exceeding 50 watts at 45 K. The Hybrid system requires two separate compressors and draws a total of approximately 3 kW.

A dual-opposed piston compressor drives the Stirling cryocooler, while the second drives the cryo-fan that circulates the cold helium gas. Although the simplicity and development maturity of the hybrid cooler are clear advantages, mass estimates (not reported) are expected to be high. Continued conversations with SHI Cryogenics will be pursued during Phase II investigations to assess the suitability of the hybrid cooler for the CREW HaT system.

5. Mechanical Support Structure

5.1 Executive Summary

In this section, the preliminary design for the coils' mechanical support structure will be discussed. The main aim of this design is to secure the superconducting coils around the spacecraft. As per the strategy mentioned in Section 2, we have performed the initial engineering design, considering the proton transmission probability computed with the aim of reducing its flux by about 50% at 600 MeV (as shown in Figure 3.8). With this requirement directly affecting the total electric current flowing in the coils, the induced magnetic forces were determined to be in the range of 10-20 MN, serving as the primary design constraint for the supporting structure.

Two different force distributions characterized by their resultant force vectors occur in the system: compressive resultant forces act on half of the electromagnets, while tensile resultant forces act on the other half. We prioritized designing around the structure's loading conditions rather than simply reducing the mass, as the winding packs of the superconducting coils hold most of the CREW HaT's mass. The internal coil support structure must counteract expansion from the hoop forces and local displacements from the inter-coil forces to within hundredths of millimeters, as the superconducting winding pack demands. This requirement was the main focus of the current phase of the design. We were able to reduce the overall displacement of the entire structure to about 1 mm by iterating through different structural designs.

We followed a similar iteration procedure regarding the coil support mounting system onto the spacecraft. Starting from the scissor beams of our benchmark design that motivated this Phase I design, we proceeded with modifications. The requirements on the displacement led us to prioritize a straight beam design with no movable components. Given the dimensions of the Starship, we discarded the folding functionality to prioritize structural stability.

The information gained during the Phase I design iterations will guide our next stage toward advanced topology optimization techniques for refining the design of the coil support structure.

5.2 Induced Inter-coil Forces

In Section 3.2, we mentioned that two force distributions are induced by the current in the coils, which serve as the primary mechanical design constraints. The inter-coil forces depend on the orientation of the electromagnets. Electromagnets perpendicular to the spacecraft (known as radial coils) experience an inward net force towards the array's center (i.e., compressive force). In contrast, the electromagnets parallel to the spacecraft (known as tangential coils) experience a complex force distribution. This complex loading results in the coils bending into the shape of a hyperbolic paraboloid, similar to a "Pringle chip." These pringle-like forces have two effects: internal bending moments that act to fold the coil and a

net linear force away from the center of the array (i.e., tensile force). You can see these forces illustrated in Figure 5.1.

The calculated tensile and compressive forces are about 11.1 MN and 17.6 MN, respectively. It's worth noting that these values are subject to change depending on the amount of current running through the superconductor and its length (equation 3.5), although the order of magnitude will likely remain the same.

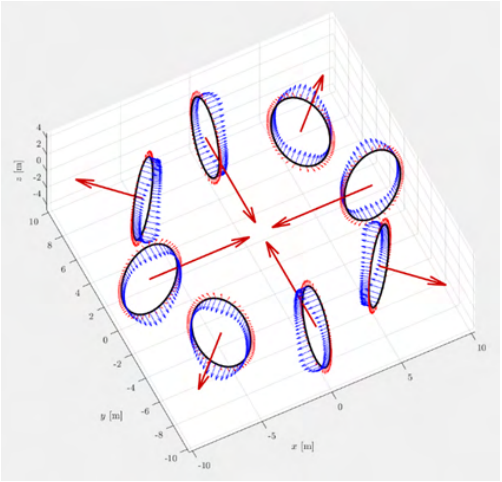

Figure 5.1: Inter-coil forces (light red), resultant force (dark red), and magnetic field on each coil (blue) in the Halbach array.

5.3 Mechanical Support Design.

In Phase I, the main goal was to replicate the force distributions induced on a CORC coil supported structurally (refer to Section 4.6.2). When modeling the compressive forces on the radial coils, we found it easier to do so in SolidWorks. However, we used Ansys Workbench to simulate the pringle-like forces on the tangential coils. Despite our efforts to find an equation for the pringle forces by making the force vectors into a 3-dimensional curve, we decided to simplify the distribution by considering them as point loads.

5.3.1 Internal Coil Support Designs

The objective of the coil's support structure was to minimize deflection by optimizing its design. Initially, we aimed to create supports that could withstand both shear compressive and pringle force distributions. However, we later focused on designing supports mainly for the compressive load. The ellipse-shaped coils, which were created using SolidWorks, have a major radius of 4 meters and a minor radius of 2 meters. For our first design, we used a honeycomb pattern that was inspired by its use in military tires known for their ability to withstand substantial compressive loads in military-grade vehicles [56]. We also considered

radiative heating and aimed to minimize the surface area of the support structure (as shown in Figure 5.2).

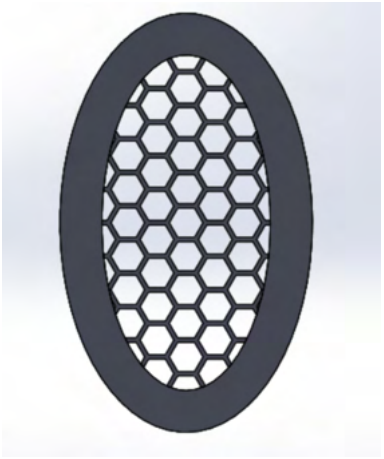

Figure 5.2: Second iteration of the honeycomb pattern to reduce surface area.

It was found that when simulating the honeycomb structure under a compressive load of 17.6 MN, the displacement measured was 2.332 mm, which exceeded the goal of 0.02 mm imposed by the superconducting coil design. A 5-bar design was introduced to mitigate this issue, as shown in Figure 5.3. This design helped to limit the deflection and almost halved the overall displacement to 1.210 mm.

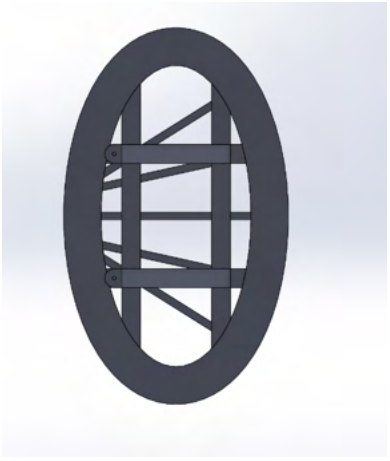

Figure 5.3: 5-bar design to prevent inward coil collapse.

We were still far from achieving our goal, so we decided to simulate a 7-bar iteration. This resulted in an overall displacement of 1.099 mm. To improve on this, we tweaked the structure's bars to converge outside the coil's radius. This led to the lowest overall displacement of 1.044 mm. Figure 5.4 displays both of these designs.

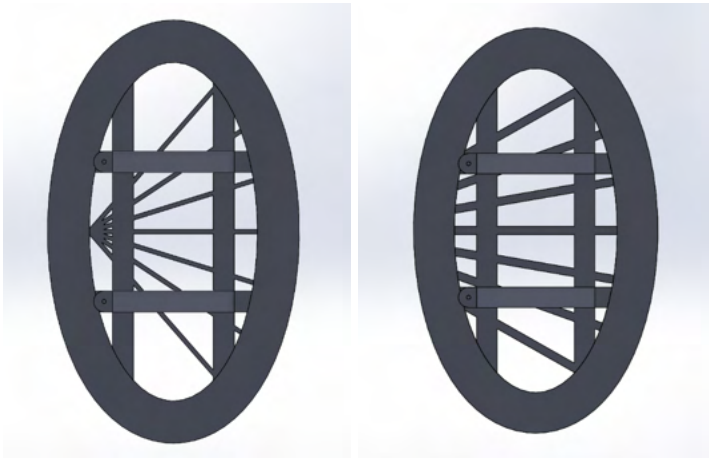

Figure 5.4: 7-bar design that converges at the center on the left side of the coil (left-hand side) and 7-bar design with supports that converge at a point outside of the coil (right-hand side).

The finite element analysis (FEA) used to evaluate the structural integrity of these iterated designs is further explained in Section 5.3.4.

5.3.2 Radial Coil Support Designs

We initiated the design process for the spacecraft's radial coil supports with a modified CREW HaT design [54, 35]. The modified design had flat ends and was adjusted to new parameters, as shown in Figure 5.5.

Figure 5.5: Edited Scissor Beam configuration from the benchmark CREW HaT Design [29, 35].

We conducted structural simulations to verify that the beams can endure the highest tensile and compressive forces. As the displacements were beyond the acceptable limit, we redirected our attention to the design of individual beams before constructing the entire

configuration. We then improved the individual beam design by making it more rounded with a thinner profile. You can see the updated design in Figure 5.6.

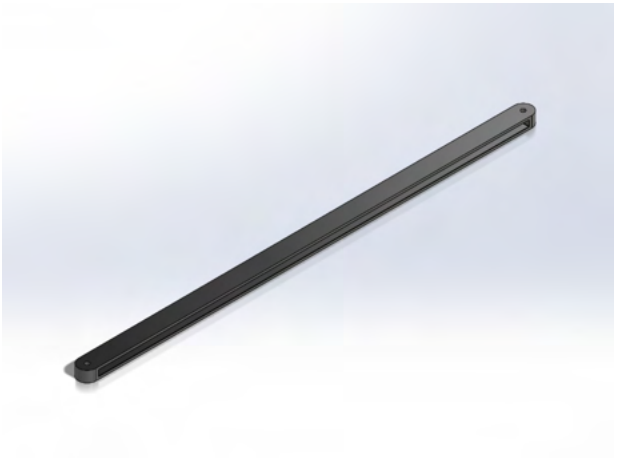

Figure 5.6: Edited I-Beam design.

We eventually incorporated the refined I-beams into the coil design for radial loads (Figure 5.7), replacing the previous scissor-like beams with four straight beams.

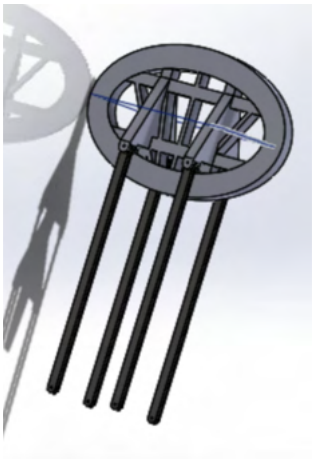

Figure 5.7: 4-beam configuration and coil combination.

5.3.3 Base Plate and Mounting Designs

We had initially planned to create a design for mounting the supports to the coils using a base plate attached to the ship. However, since we have not yet determined the deployment methods, we have shifted our focus to the internal coil supports. The current mounting geometries are basic and are being used as placeholders to allow the analysis to continue.

These mounts are designed in SolidWorks and can be easily adapted to any changes in the coil support geometry. As there are two coil configurations, radial and tangential, two corresponding mounting geometries are required (as shown in Figure 5.8).

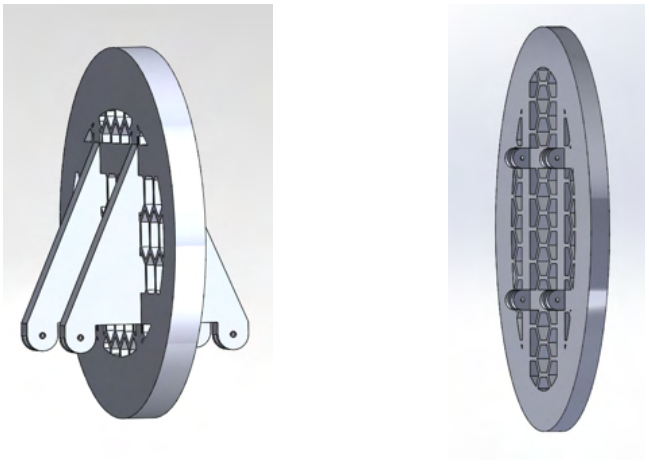

Figure 5.8: Initial mounting design for radial coil (left) and tangential coil (right).

We have conducted an investigation into designing a simple mounting structure that can be used to attach the assembly's base to the spacecraft. The mounting structure is made of large aircraft-grade aluminum sheets that conform to the MIL-T-81556 standard for high-quality titanium and titanium alloy extruded metal products. The design of these sheets is illustrated in Figure 5.9.

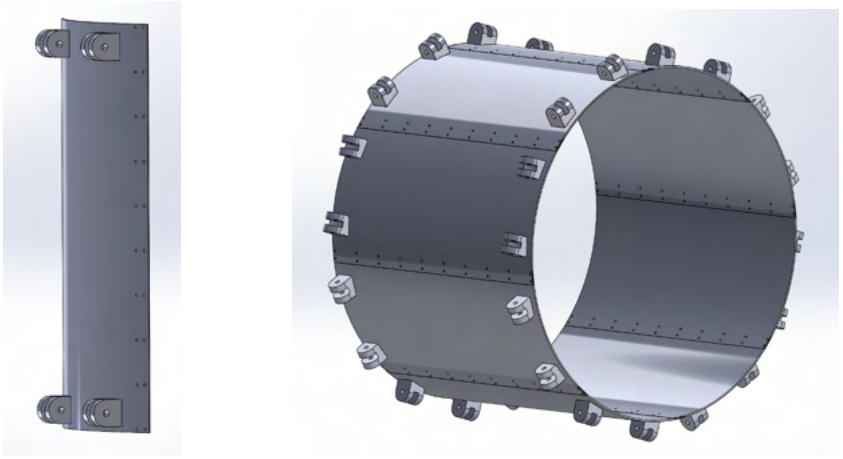

Figure 5.9: Initial mounting design for base plate (left) and assembly of 8 base plate structures (right).

Although the preliminary mounting design is not complex at this project stage, it provides the fixed points needed for computing finite element analyses on the overall structure.

5.3.4 Finite Element Analysis in Solidworks and Ansys Workbench

We used SolidWorks and Ansys due to their suitability for varying force distributions – SolidWorks for compressive loads and Ansys for pringle force loads.

5.2.4.1 Internal Coil Support - Compressive Force Analysis

In order to replicate the previously calculated compressive resultant force of 17.6 MN, a uniform inward "gravitational force" was applied to the assembly, as depicted in Figure 5.10. This accurately simulates the force acting on the entire coil body. The materials used for the Finite Element Analysis (FEA) were 1023 Carbon Steel for the coils and 6061 T6 Aluminum for the support structures, which ensures a significant density difference.

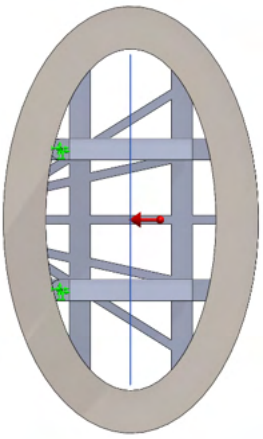

Figure 5.10: Applied gravitational force on a coil undergoing a load of 17.6 MN.

In the design process, three different designs were evaluated (see Figures 5.2, 5.3, and 5.4). The honeycomb design of Figure 5.2 had an excessive displacement of 2.332 mm. The 5-bar design of Figure 5.3 reduced displacement to 1.210 mm, and the 7-bar design of Figure 5.4 achieved a maximum displacement of 1.044 mm, making it the current best design (see Figure 5.11). However, none of the designs achieved the goal of a maximum displacement of 0.02 mm. Despite this, the reduction in displacement observed in the design process is promising.

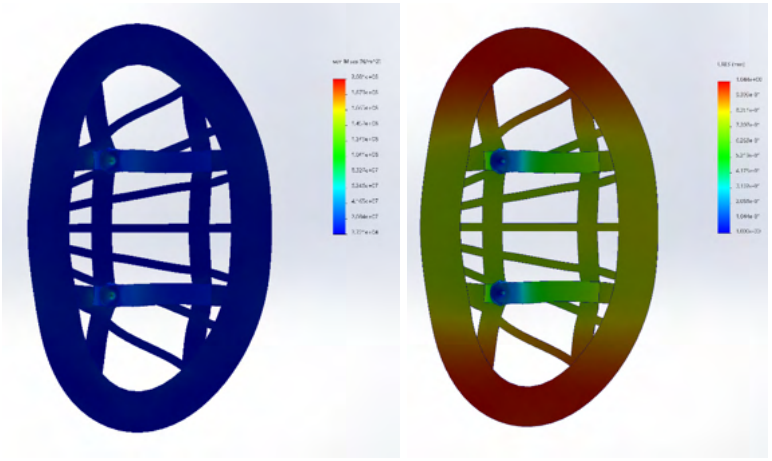

Figure 5.11: FEA for 7-bars converging to a point outside of the coil. Displacements not in scale.

5.2.4.2 Radial Coil Support Analysis

Radial coil supports were implemented to minimize displacement and ensure safety. Initially, the scissor beam approach was modified but was found to be insufficient. Even with isolated I-beams, high deformation was still observed, leading to further geometry changes. Ultimately, the final design comprised four straight beams, as depicted in Figure 5.12. When subjected to compression, these beams resulted in a small displacement of only 12.79 mm.

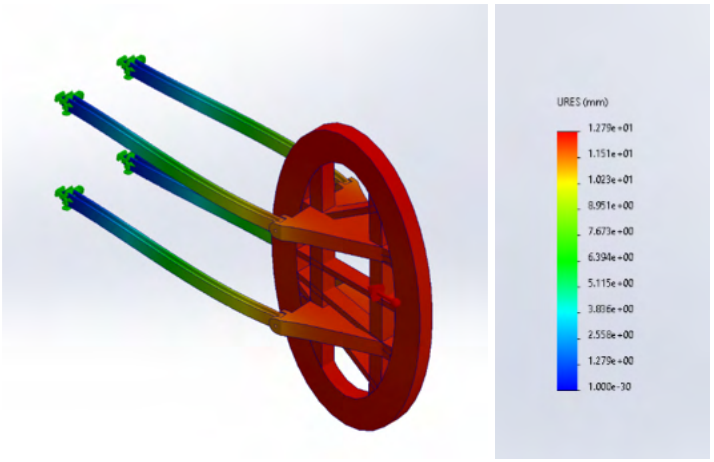

Figure 5.12: Displacement results for a combination of coil and beams.

Further development is required at connection points due to the high-stress concentration shown in Figure 5.13.

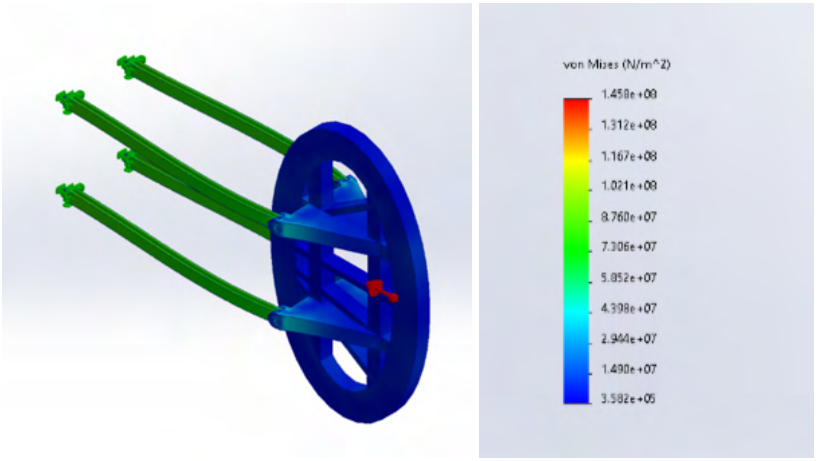

Figure 5.13: Stress analysis for a combination of coil and beams.

During the Phase I initial design process, it was discovered that addressing the structure's specific and precise loading conditions is crucial rather than just focusing on reducing weight. When analyzing structures with reduced weight under complex and substantial loading, it is important to consider all aspects of the design. This is why more advanced techniques, such as topology optimization, are being utilized to help design the coil support structures. The next iterations of the coils' mechanical support design will incorporate these new analyses.

6. Radiation Exposure

6.1 Executive Summary

This section describes the framework we developed to estimate the whole-body equivalent radiation dose a crew would be exposed to during a three-year mission to Mars. The framework utilizes the Geant4 particle physics Monte Carlo simulation software, which computes collisions of GCR particles with a spacecraft to generate secondary particles and energy deposits of these "particle cascades" in the matter they traverse. The International Commission on Radiological Protection (ICRP) Adult Male Computational Phantom (ICRP 110) is used to estimate the radiation exposure on the human crew, representing the realistic human body with all its internal organs. The energy deposited on each organ is recorded and converted into an equivalent dose via radiation weighting factors, which allows the fluence-to-dose conversion coefficients to be calculated.

Our simulation framework employs a technique called "Importance Sampling", which is a type of Monte Carlo method used to evaluate the properties of a specific distribution using samples generated from a different distribution. This allows us to generate GCR particle beams with an unphysical generic energy distribution only once and then re-weight them to suit different physical situations.

This Monte Carlo method enables us to estimate the radiation dose during Solar Maximum and Minimum by implementing different GCR fluences in our weighting functions. The effect of the CREW HaT active magnetic shielding is also evaluated using a weighting function based on the proton transmission probability calculated with our numerical particle trajectory integration (see Section 3).

We used the Geant4 simulation package to evaluate the whole-body equivalent dose a crew would be exposed to in open space for different passive and active shielding scenarios. Our estimates show that the equivalent dose during Solar Maximum is about half that during Solar Minimum (where GCR flux is three times as high). Given the proton transmission probability of Figure 3.8 that corresponds to our CREW HaT "geometry configuration benchmark" (Section 3.2) extrapolated to a generic GCR particle type via equation (3.4), we estimate that our preliminary active magnetic shielding system produces a radiation dose reduction equivalent to a combination of aluminum and polyethylene passive shielding layers with an excess mass of approximately 100 tons.

The current Phase I CREW HaT design, based on our preliminary geometry configuration benchmark and designed to be adapted to SpaceX Starship, has a total mass of about the same order of magnitude. Our next steps are to proceed with the iterative strategy outlined in Section 2 using our finalized computational framework to find the best CREW HaT geometry configuration capable of reducing the whole-body equivalent dose to no more than 200 mSv/year (for a three-year mission to Mars) with a total mass that is smaller than that of a passive shielding providing the same mitigation.

6.2 Context and Aim

Exposure to radiation in space is a significant concern for astronauts as they venture beyond the protective shield of Earth's atmosphere and magnetic field. In the vast expanse of space, astronauts are subjected to various high-energy particles, including SPEs from the Sun and GCRs from outside our solar system. These particles can penetrate spacecraft hulls and the human body, potentially causing a range of health issues, from acute effects like radiation sickness to long-term consequences such as increased cancer risk and damage to the cardiovascular and nervous systems [69-71].

In Phase I of this project, we sought to investigate radiation exposures to astronauts as a result of extended space missions beyond the low earth orbit. Our work aims to provide preliminary insight into the benefits of adding the CREW HaT active shielding system to protect astronauts inside the crew module of a spacecraft. We considered eight different shielding scenarios:

1. Free Space (i.e., astronauts in the vacuum of space),
2. 20 g/cm^2 Al (aluminum) hull,
3. 20 g/cm^2 Al hull, and 5 g/cm^2 PE (polyethylene),
4. 40 g/cm^2 Al and 10 g/cm^2 PE,
5. CREW HaT active shielding alone,
6. CREW HaT active shielding in addition to 20 g/cm^2 Al hull,
7. CREW HaT active shielding in addition to 20 g/cm^2 Al hull and 5 g/cm^2 PE.
8. CREW HaT active shielding in addition to 40 g/cm^2 Al and 10 g/cm^2 PE

6.3 Monte Carlo Simulations

6.3.1 GCR Particle Simulations

To represent the GCR particle flux that impinges on the crew module and astronauts, we leveraged the ability of Monte Carlo simulations to perform discrete-event computations for each particle type considered. Our Monte Carlo simulation aims to reproduce the radiation environment of a spacecraft crew during interplanetary travel. To do so, we started with approximations that allowed us to compute radiation exposure estimations under the scenarios outlined in Section 6.2.

The spacecraft crew module was modeled as a hollowed sphere, and a whole-body computational phantom was used to model an astronaut. Figure 6.1 illustrates the geometry used in our simulations. We used the ICRP Adult Male Computational Phantom (ICRP 110) [57], shown in Figure 6.1-A. The Adult Male phantom has a weight of 73 kg and contains 140 unique organs. Our choice to use an anthropomorphic computational phantom over a traditional tissue sphere phantom was influenced by NASA’s interests in better understanding

latent (e.g., cancer) and acute (e.g., neurological and cardiovascular) effects of ionizing radiation from long space missions [7]. This reasoning is supported by NASA's recent mission that sent two anthropomorphic physical phantoms (Helga and Zohar) [58] on a 25-day space mission around the moon aboard the Artemis/Orion crew module.

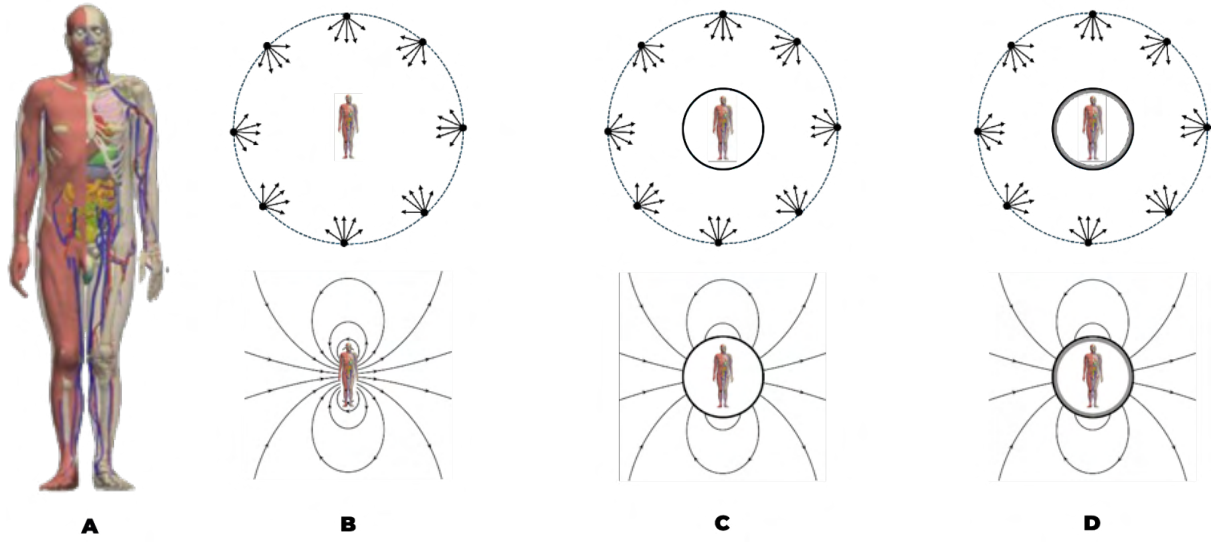

Figure 6.1: Simulation geometries used for dose calculations for the eight scenarios considered. The ICRP 110 adult male computational phantom (A) was placed in the center of a large sampling sphere with an isotropic GCR particle field in a vacuum volume of space. The free space simulations and the simulations involving CREW HaT active magnetic shielding are represented in B. The simulation geometries that implemented an Al passive shielding shell (containing air and the computational phantom and representing a "spacecraft") and active shielding are illustrated in C. The simulations implementing the Al "spacecraft" hull and additional PE passive shielding without and with active shielding are illustrated in D.

We produced a series of mono-energetic "beams" of GCR particles, with uniform and isotropic directions on a large "sampling sphere" around the computational phantom, as shown in Figure 6.1. The free space simulations (i.e., of an astronaut in the vacuum of space) and the simulations involving CREW HaT active magnetic shielding are shown in Figure 6.1-B (representing scenarios 1 and 5 of Section 6.2). The simulation geometries that implemented an aluminum (Al) passive shielding shell (containing air and the computational phantom and representing a "spacecraft") without and with active shielding are illustrated in Figure 6.1-C (scenarios 2 and 6). The simulations implementing the Al "spacecraft" hull and additional Polyethylene (PE) passive shielding layer without and with active shielding are illustrated in Figure 6.1-D (representing scenarios 3, 4, 7, and 8).

In this Phase I work, we produced extensive simulation data of 5 GCR particles representing the relatively most abundant "mass groups" (see Figure 6.2), such as protons (H), ^{4}He, ^{12}C (representative of the so-called "CNO mass group"), ^{28}Si (representative of the so-called "NeMgSi mass group"), and ^{56}Fe. Mass groups represent similar-mass elements with comparable abundance in GCRs.

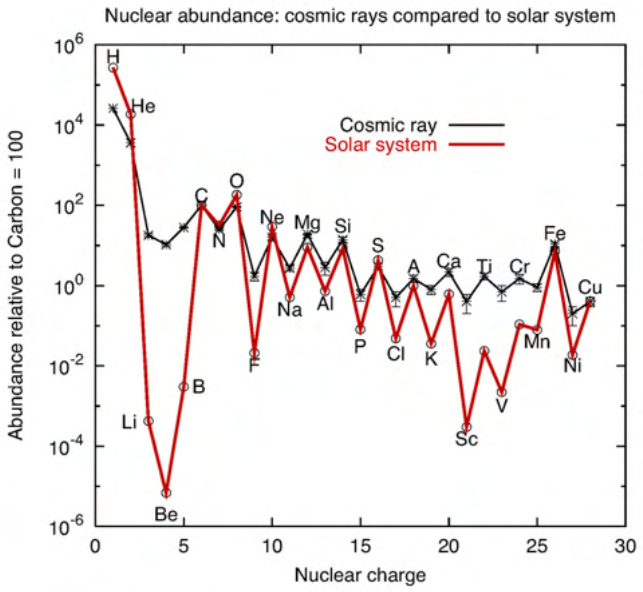

Figure 6.2: Nuclear abundance in GCRs compared to the Solar System [59]. The relatively more abundant nuclei are H, He, C-N-O, Ne-Mg-Si, and Fe. The differences in nuclear abundance between GCRs and the Solar System are due to the long propagation time of GCR particles across the Milky Way and the chance of colliding with interstellar matter and producing a higher abundance of secondary nuclei.

We performed our computations using the Geant4 (v11.1) simulation package [60-62]. Geant4 is a toolkit developed at the "European Organization for Nuclear Research" or "Conseil Européen pour la Recherche Nucléaire" (CERN) [63], an international high-energy particle laboratory located in Geneva, Switzerland. Geant4 uses Monte Carlo computational methods to simulate the passage of particles through matter. It is been used in a variety of applications. From reproducing high-energy particle collisions and fragmentations to propagation through matter, including energy losses. From nuclear physics investigations to designing medical physics radiation monitoring devices. From space science research to space engineering design. Applications built in the Geant4 package can simulate any setup or detector and radiation source. They can also record a chosen output of physical quantities due to source particles and secondary particles interacting with the material of the setup.

With Geant4, we produced a series of mono-energetic "beams" of each of the aforementioned five representative GCR particle types, with uniform and isotropic directions on a "sampling sphere" around the computational phantom (Figure 6.1). Since the energy spectra of these GCR particles span several orders of magnitude, we chose to discretize each spectrum into independent energy bins. A total of 125 energy bins were selected, uniformly spanning from $E_{min} = 10^{-2}$ MeV/nucleon to $E_{max} = 1 \times 10^{6}$ MeV/nucleon (in $log10(E)$ scale, i.e., each energy bin has a width of $\Delta log10(E) = 0.064$).

For each of the five chosen representative GCR particle types, we generated simulation sets for all the shielding scenarios considered to compute the "whole-body absorbed dose" $D(E, particle)$ (in units of Gy/particle/MeV/n) and the "whole-body equivalent dose" $H(E, particle)$ (in units of Sv/particle/MeV/n) per source particle per energy bin.

6.3.2 Calibrating with ICRP 116 Simulation Benchmark

To calibrate our Geant4 Monte Carlo computational set-up, we ran a simulation with infinitesimally thin protons beam in the vacuum at different discrete energies from 10 MeV to 10,000 MeV impinging on the gonads organ of the computational phantom. We evaluated the corresponding absorbed dose, which measures the energy deposited in the organ per unit of mass (expressed in units of Gray, or Gy = Joules/kg). We then compared the gonad absorbed dose per proton fluence received by the phantom to the ICRP 116 publication benchmark data [68].

Figure 6.3 shows an illustration of the proton trajectories hitting the gonads (panel A) and the absorbed dose per fluence we computed with Geant4 (in red) compared to the ICRP 116 reference (in black) in panel B.

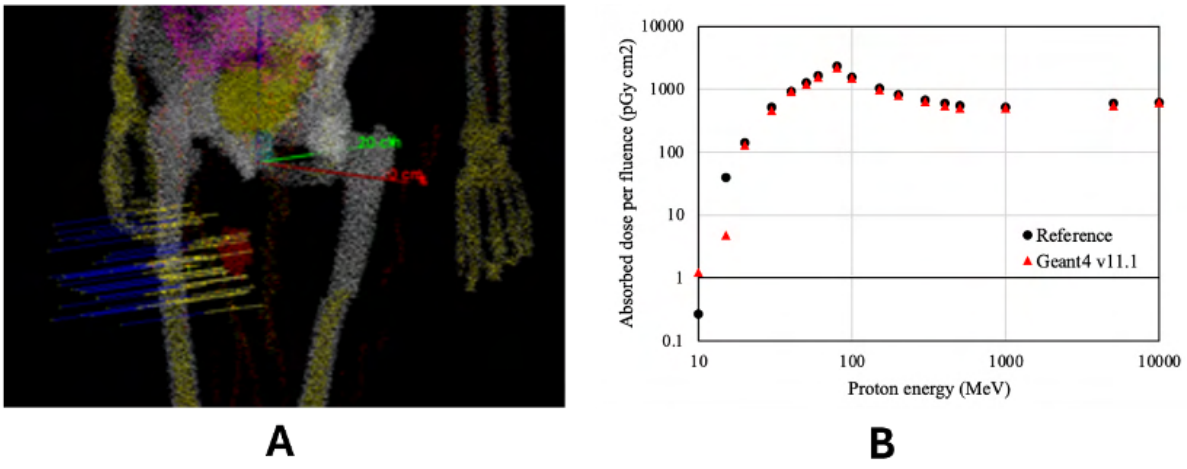

Figure 6.3: Benchmark simulations using ICRP 103 adult male phantom. The gonad dose per fluence received by the phantom was compared to previously published data from the ICRP [68].

Our Geant4 simulation framework is thus properly calibrated by comparing it with the ICRP 116 reference benchmark. This gives us confidence that our particle physics computations are correct.

6.3.3 Radiation Weighting Factors

In radiation protection, the concept of the radiation weighting factor, w_R, was initially introduced in the ICRP Publication 60. Subsequently, it was embraced by the National Council of Radiation Protection (NCRP) Publication 116 and underwent further redefinition in the subsequent ICRP Publication 103.

The equivalent dose is defined as $H = \Sigma w_R D_R$. Notably, the w_R factors (shown in Table 6.1) remain independent of linear energy transfer (LET) and are determined by the attributes of the external radiation environment. Consequently, a characteristic of the definition of equivalent dose emerges: while the absorbed dose, D_R, is contingent upon the internal

radiation context, w_R, as previously noted, is contingent upon the external radiation environment. Consequently, in the simulation, radiation weighting factors were determined outside the phantom, and the ensuing weights were allocated for subsequent internal radiation interactions.

Types and energy range of incident radiation	Radiation weighting factor (w_R) in ICRP 103
Photons, all energies	1
Electrons and muons (all energies)[a]	1
Protons (incident)	2
Neutrons	$w_R = \begin{cases} 2.5 + 18.2 \cdot e^{-[\ln(E_n)]^2/6}, & E_n < 1\ MeV \\ 5.0 + 17.0 \cdot e^{-[\ln(2 \cdot E_n)]^2/6}, & 1MeV \le E_n \le 50\ MeV \\ 2.5 + 3.25 \cdot e^{-[\ln(0.04 \cdot E_n)]^2/6}, & E_n > 50\ MeV \end{cases}$
Alpha particles, fission fragments, and heavy ions[b]	20

a. Exclude Auger electrons from emitters localizing to cell nucleus/DNA-special treatment needed.
b. Use Q-LET relationships of Publication 60 for unspecified particles.

Table 6.1: Radiation weighting factors to each incident radiation type and energy in ICRP Publication 103.

6.4 Equivalent Dose Calculation

The equivalent dose, which also measures the amount of energy deposited per unit of mass (measured in Sievert, or Sv), accounts for each incident particle's different relative biological effectiveness and is calculated by applying the radiation weighting factors of table 6.1 to the external radiation field incident on the phantom. For each simulation set, enough particles were simulated so that the relative error for each dosimetric quantity was less than 5%.

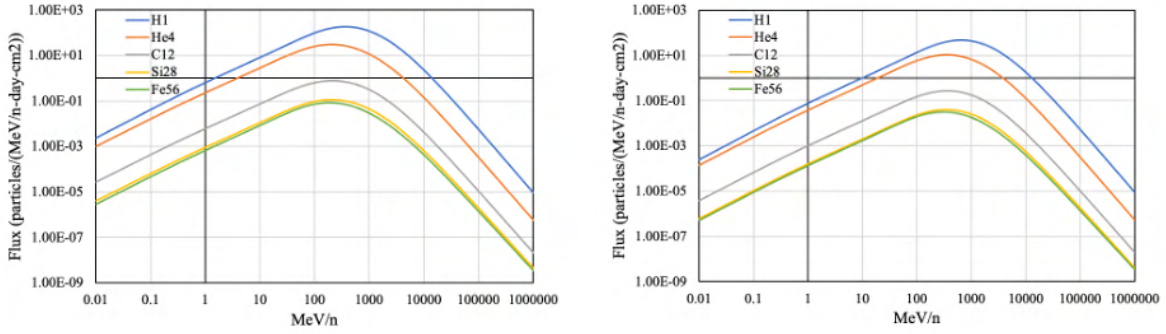

Figure 6.4: GCR particles energy spectrum for H, ^{4}He, ^{12}C, ^{28}Si, and ^{56}Fe during the Solar Minimum 2010 (on the left) and the Solar Maximum 2001 (on the right, when the GCR flux is about three times lower). The fluxes are from the Badhwar-O'Neill 2014 model [36] and retrieved through the NASA On-Line Tool for the Assessment of Radiation In Space (OLTARIS) [64, 65].

The annual whole-body absorbed dose (Gy/year) and whole-body equivalent dose (Sv/year) were determined by convolving $D(E, particle)$ and $H(E, particle)$ with the GCR flux data (see Figure 6.4) at both Solar Minimum and Solar Maximum. The flux data are from

the Badhwar-O'Neill 2014 model [36]. The same weighting scheme was used to determine the doses corresponding to the CREW HaT active magnetic shielding turned on by simply convolving the dose quantities with the transmission probability curve from Figure 3.8. Note that the modified energy spectrum created by the CREW HaT active magnetic shielding (see Section 3) was calculated using the particle trajectory numerical integration described in [66].

All annual doses were compared to NASA's annual "effective dose" lifetime exposure limit of 600 mSv/yr, assuming the doses were deposited uniformly throughout the body [7, 67].

6.5 Results

The results of each shielding scenario are provided in Table 6.2. Figure 6.5 graphically illustrates the whole-body equivalent dose for the shielding scenarios considered. Note that the estimated absorbed dose and equivalent dose from NASA's OLTARIS [58, 65] in free space are 102 mGy/year and 428 mSv/year at Solar Minimum, respectively. Differences can be explained by the type of computational phantoms used, the different radiation weighting factors, and the different radiation transport methods used to calculate the dosimetric results.

Note that the whole-body equivalent dose (mSv/year) corresponding to the "Free Space in vacuum" reported in Table 6.2 was derived by manually calculating from the absorbed dose (mGy/year) using the respective radiation weighting factors in Table 6.3 (for Solar Minimum). The same calculation is done in the Solar Maximum case. This approach assumes an ideal scenario where every initial GCR particle enters and interacts with the whole body ICRP computational phantom with its corresponding radiation weighting factor. We use the approximation only in the free space scenario because no incident secondary particles need to be accounted for. For other shielding scenarios, we explicitly compute the whole-body equivalent dose via radiation weighting factors.

During Solar Maximum, the equivalent dose is about half of that at Solar Minimum and below 200 mSv/year for all shielding scenarios except free space. This upper limit is necessary in order to comply with the 600 mSv career limit for a three-year mission to Mars (assuming that the shielding scenarios are applicable to the entire mission). The CREW HaT's benchmark magnetic shielding system from Section 3.2, described in this report, reduces the GCR flux at lower energy according to the transmission probability of Figure 3.8.

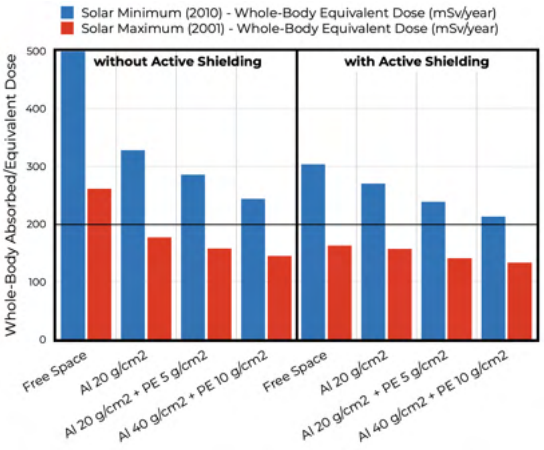

Figure 6.5: Graphical representation of the estimated whole-body equivalent dose (mSv/year) from Table 6.1. The blue bars indicate the equivalent dose during the Solar Minimum, and the red bars during the Solar Maximum. The horizontal line at 200 mSv/year is the upper limit corresponding to NASA's 600 mSv lifetime exposure limit in a three-year mission to Mars.

Shielding Scenario	Solar Minimum 2010			Solar Maximum 2001		
	Whole-Body Absorbed Dose (mGy/year)	Whole-Body Equivalent Dose (mSv/year)	Equivalent Dose Reduction	Whole-Body Absorbed Dose (mGy/year)	Whole-Body Equivalent Dose (mSv/year)	Equivalent Dose Reduction
without CREW HaT active magnetic shielding						
Free Space in vacuum	**60**	**500**		**29**	**261**	
Al 20 g/cm^2	**86**	**328**		**48**	**177**	
Al 20 g/cm^2 + PE 5 g/cm^2	**86**	**286**		**50**	**158**	
Al 40 g/cm^2 + PE 10 g/cm^2	**93**	**244**		**57**	**145**	
with CREW HaT active magnetic shielding						
Free Space in vacuum	**46**	**304**	**-40%**	**25**	**163**	**-38%**
Al 20 g/cm^2	**71**	**270**	**-18%**	**44**	**157**	**-11%**
Al 20 g/cm^2 + PE 5 g/cm^2	**73**	**239**	**-16%**	**45**	**141**	**-11%**
Al 40 g/cm^2 + PE 10 g/cm^2	**82**	**213**	**-13%**	**53**	**133**	**-8%**

Table 6.2: Results of simulations representing each shielding scenario for solar minimum and solar maximum GCR fluxes.

GCR particle	absorbed dose (mGy/year)	equivalent dose (mSv/year)	radiation weighting factor
H	38.8	77.6	2
He	15.1	301.2	20
C	2.2	44.9	20
Si	1.3	26.1	20
Fe	2.5	49.7	20
Total	**59.9**	**499.5**	

Table 6.3: Calculation of whole-body equivalent dose from absorbed dose in the “Free Space in vacuum” scenario during Solar Minimum.

Figure 6.6 shows the whole-body equivalent dose reduction inside an Al 20 g/cm^2 passive shielding hull as a function of the GCR particles' energy. The Al layer provides a reduction of the equivalent dose from, e.g., protons of 50% at about 200 MeV/n and no protection above 300 MeV/n. With the CREW HaT active shielding turned on, lower energy protons are diverted back to space, reducing the crew’s exposure effects. The proton 50% equivalent dose reduction mark extends to about 400-500 MeV/n. Heavier GCR particles produce more secondary particles, thus contributing to a limited dose reduction at high energy. The overall exposure is reduced by about 20% (see Table 6.2).

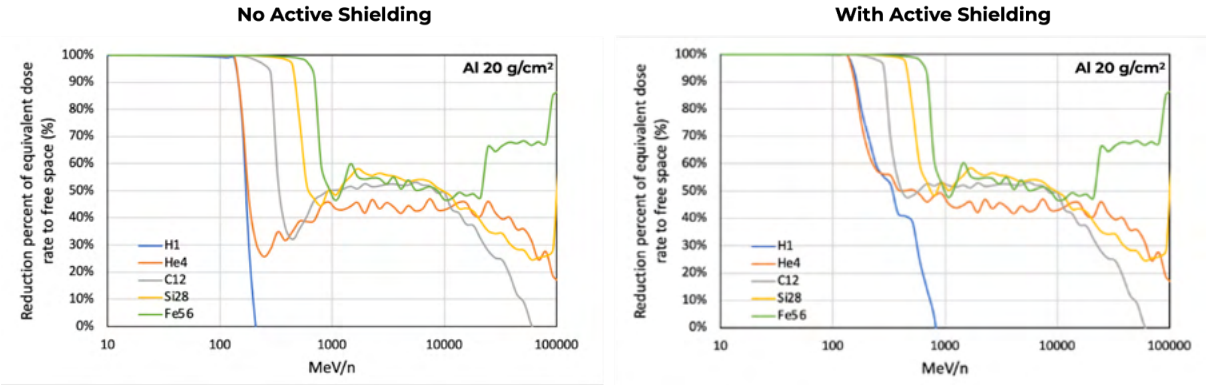

Figure 6.6: Reduction of the whole-body equivalent dose estimated in the shielding scenario with Al 20 g/cm^2 hull due to the passive shielding only (on the left) and the additional CREW HaT active magnetic field (on the right) at Solar Maximum.

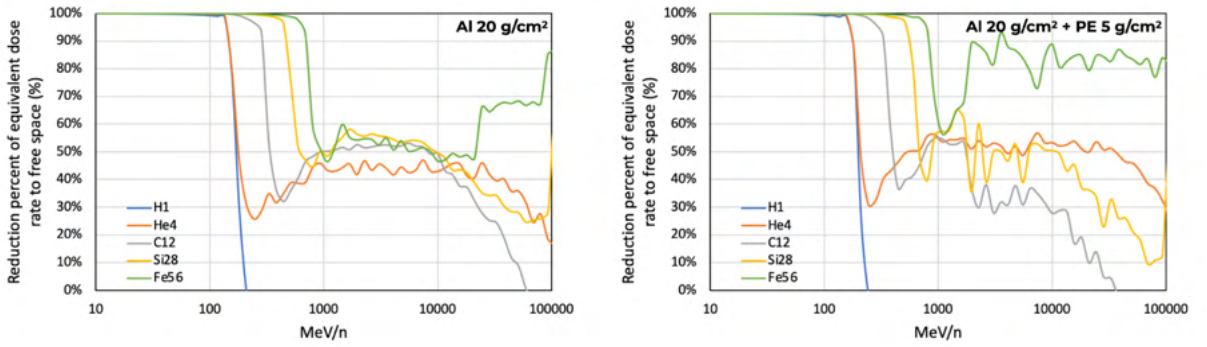

Figure 6.7: Reduction of the whole-body equivalent dose estimated in the passive shielding scenario with a layer of Al 20 g/cm^2 (on the left) and with additional Polyethylene 5 g/cm^2 (on the right) at Solar Maximum. No active shielding is used in this figure.

Figure 6.7 shows that an additional passive shielding layer with a low-Z material, i.e., a light-mass atomic composition such as polyethylene, significantly enhances equivalent dose reduction at high energy. This is because materials such as polyethylene and water effectively absorb particles and thermalize secondary neutrons.

Table 6.2 and Figure 6.5 show that a passive shielding composed of Al 40 g/cm^2 + PE 10 g/cm^2 is equivalent to a thinner passive shielding (i.e., Al 20 g/cm^2 + PE 5 g/cm^2) with the active magnetic shielding turned on. If we assume that the StarShip's crew habitat occupies an 8-meter section, we can estimate that the CREW HaT's active magnetic shielding is approximately equivalent to an additional 100 tons of passive shielding. This investigation also highlights that the proper choice of a combination of active and passive shielding is the only viable way to achieve our goal with more relaxed engineering constraints on the CREW HaT. Lower coil currents mean smaller magnetic forces, leading to fewer load and strength requirements and, therefore, smaller mass. We now have all the tools in place to carefully investigate how our CREW HaT system's requirements scale depending on the application contexts.

7. Conclusions and Discussion

In this report, we present the findings of our Phase I feasibility study on an open-geometry active magnetic shielding system designed to mitigate GCR radiation exposure during long-duration space missions. Our primary objective in Phase I was to define the CREW HaT configuration geometry that provides optimal protection from solar wind and galactic cosmic rays by minimizing radiation exposure and the magnetic forces exerted on the support structure. However, our focus shifted when we considered the challenges of shielding a crew during a three-year interplanetary mission to Mars instead of protecting a human habitat designed for the International Space Station or Lunar Gateway. We assumed that CREW HaT would be docked onto SpaceX Starship and developed an investigation strategy and initial working parameters to reduce GCR proton flux to 50% at 600 MeV/n.

We numerically integrated particle trajectories through CREW HaT's magnetic field with a custom-developed software code to determine the geometry configuration and magnetic field strength necessary to satisfy our initial condition. We then used our obtained CREW HaT geometry configuration benchmark to develop the engineering design of the superconducting electromagnet, its structural casing, and the support mechanical structure to keep the coils in place around the spacecraft. Additionally, we implemented the Geant4 numerical framework to evaluate the whole-body radiation equivalent dose that a long-duration deep space mission crew is exposed to, based on the ICRP computational human phantom, calibration benchmarks, and definitions.

In the initial phase of our project, we focused on refining the CREW HaT magnetic shield design to significantly mitigate radiation exposure for astronauts, relying solely on the capabilities of the magnetic shield. A notable success of the CREW HaT's active shielding was its ability to outperform traditional aluminum passive shields, cutting the radiation dose from protons at 400-500 MeV/n by half and reducing total GCR exposure by 20%, thus offering enhanced protection. These outcomes were precisely measured using comprehensive Monte Carlo simulations within the Geant4 framework, utilizing the ICRP110 human phantom and covering an energy spectrum from 1 MeV/n to 100 GeV/n. Our findings indicated whole-body equivalent radiation doses of 0.4 mSv/day during the Solar Maximum and 0.8 mSv/day during the Solar Minimum, achieving a milestone beyond NASA's benchmark for a 15% reduction in GCR radiation dose in open space. For a three-year Mars mission during the Solar Maximum, our magnetic shield could lower astronaut radiation exposure to around 160 mSv/yr, placing well below NASA's lifetime limit of 600 mSv for astronaut exposure, highlighting the effectiveness of our approach for extended space travel.

Our methodology involved an intricate process of selecting and fine-tuning the superconductor coil designs for the eight coils in the Halbach array. This stage included evaluations and selections among commercially available superconductors, focusing on their electrical performance, heat resistance, and length. Kevlar and Carbon-fiber composites emerged as top material choices, able to withstand magnetic forces up to 10 Tesla. We also examined various coil shapes for their mass efficiency, considering both circular and elliptical forms to minimize weight, an essential factor for a mission to Mars.

Despite the progress, achieving a coil mass lower than 15 tons highlighted the technical hurdles inherent in developing such sophisticated magnetic systems. Our investigations extended to all possible heat sources affecting the coils, such as solar radiation and internal heat production, to determine the required cooling capacity for stable operation. We also initiated a study on the mechanical framework needed to support these coils, including force analysis. The results from Phase I confirm the viability and promise of our magnetic shield concept in significantly boosting astronaut safety for prolonged space journeys while also suggesting the need for further exploration and improvement. The challenges and open questions, especially regarding material choice, heat management, and structural support, emphasize the need for ongoing, in-depth investigation in Phase II.

Our Phase I mechanical design study abandoned the idea of a deployable CREW HaT system to prioritize overall strength. In Phase II, we will address structural topology optimization procedures for maximal mechanical strength under the loads imposed by the magnetic forces. Our Phase I CREW HaT concept design provides adequate mitigation during Solar Maximum and a whole-body equivalent dose reduction comparable to that of an additional passive shielding (including aluminum and polyethylene layers) with a mass of approximately 100 metric tons. We will address the challenges identified in Phase I and described in this report in our Phase II study, which will lead to reduced overall mass and power consumption.

Given the design's complexity, scalability is a complex and non-linear process. The computational tools we developed during Phase I will make it possible to produce iterations of our design, from radiation exposure to active shielding geometry, from the superconducting coil arrangement to the support mechanical support structure. We explored the design requirements for lodging the CREW HaT onto the larger Starship spacecraft, which provides new logistic challenges regarding launch requirements, maneuvering, and insertion into orbit.

The active shielding system can be launched with the spacecraft or launched separately and docked in space. The details of this will be studied in future design process development. We will address the challenges identified in Phase I and described in this report in our Phase II study.

References

[1] NASA, “NASA completes Artemis Space Launch System Structural Testing Campaign”, https://www.nasa.gov/exploration/systems/sls/nasa-completes-artemis-sls-structural-testing-campaign.html.

[2] Turner, R., “Impact of Solar Cycle Duration on Astronaut Radiation Exposure during a Human Mars Mission.” 51st International Conference on Environmental Systems, Saint Paul, MN, 2022, https://ttu-ir.tdl.org/items/66cc2bdf-7d2b-4a86-acea-1825dfeacb75.

[3] NASA “SpaceRadiation” https://www.nasa.gov/sites/default/files/atoms/files/space_radiation_ebook.pdf.

[4] Lin, E.C., "Radiation risk from medical imaging", Mayo Clin. Proc., Vol. 85, 2010, p. 1142

[5] NCRP, National Council on Radiation Protection and Measurements. “Report No. 160, Ionizing Radiation Exposure of the Population of the United States.” https://ncrponline.org/publications/reports/ncrp-report-160.

[6] Zhang, Shenyi. “First measurements of the radiation dose on the lunar surface.” *Science Advances*, vol. 6, 2020, p. eaaz1334. https://doi.org/10.1126/sciadv.aaz1334.

[7] Valinia, A., et al., "Safe Human Expeditions Beyond Low Earth Orbit (L.E.O.)", NASA/TM-20220002905, NESC-RP-20-01589, 2022.

[8] Durante, M., and Cucinotta, F.A., "Heavy ion carcinogenesis and human space exploration", Nat. Rev. Cancer, Vol. 8, No. 6, 2008, p. 465.

[9] Battiston, R., et al., "Active radiation Shield for Space Exploration Missions (ARSSEM)", 2012, arXiv:1209.1907.

[10] Al Zaman, Md. A., et al., "Study on Superconducting Magnetic Shield for the Manned Long Termed Space Voyages", Egyp. J. Rem. Sens. Sp. Sci., Vol. 24, n. 2, 2021, p. 203.

[11] Norbury, J.W., et al., "Galactic cosmic ray simulation at the NASA Space Radiation Laboratory", Life Sci. Space Res., Vol.8, 2016, pp. 38-51.

[12] Hoffman, J., et al., "Use of superconducting magnet technology for astronaut radiation protection", Final Report, NIAC Phase I, Contract CP, 04-01, 2005.

[13] Spillantini, P., "Radiation Shielding of spacecraft's in manned interplanetary flights", Nucl. Phys. B-Proc. Suppl., Vol. 85, 2000, p. 3.

[14] Spillantini, P., "Active Shielding for long-duration interplanetary manned mission", 37th COSPAR Scientific Assembly, 2008, p. 2998.

[15] Spillantini, P., "Active Shielding for long-duration interplanetary manned missions", Adv. Space Res., Vol. 45, 2010, p. 900.

[16] Spillantini, P., "Superconducting magnets and mission strategies for protection from ionizing radiation in interplanetary manned missions and interplanetary habitat", Acta Astronaut., Vol. 68, 2011, p. 1430.

[17] Badhwar, G.D., and Cucinotta, F.A., "Depth dependence of absorbed dose, dose equivalent, and linear energy transfer spectra of galactic and trapped particles in polyethylene and comparison with calculations of the models", Radiat. Res., Vol. 149, 1998, p. 209.

[18] Durante, M., et al., "Cytogenic effects of high-energy iron ions: dependence on shielding thickness and material", Radiat. Res., Vol. 164, 2005, p. 571.

[19] Shavers, M.R., et al., "Implementation of ALARA radiation protection on the I.S.S. through polyethylene shielding augmentation of the service module crew quarters", Adv. Space Res., Vol. 34, 2004, p. 1333.

[20] Wilson, J.W., et al., "Issues in space radiation protection: galactic cosmic rays", Health Phys., Vol. 68, 1995, p. 50.

[21] Wilson, J.W., et al., "Shielding strategies for human space exploration", NASA CP 3360, 1997.

[22] AstroRad, https://stemrad.com/astrorad-4

[23] Vuolo, M., et al., "Exploring innovative radiation shielding approaches in space: A material and design study for a wearable radiation protection spacesuit", Life Sci. Space Res., Vol. 15, 2017, p. 69.

[24] Battiston, R., et al., "Superconductive Magnet for Radiation Shielding of Human Spacecraft", Final Report ESTEC, Contract N. 4200023087/10/NL/AF, Noordwijk, 2011.

[25] Westover, S.C., et al., "Magnet Architectures and Active Radiation Shield Study (MAARSS)", NASA Innovative Advanced Concepts (NIAC), 2013, Phase I, Final Report & 2019, Phase II, Final Report.

[26] Calvelli, V., et al., "The limits of space radiation magnetic shielding: an updated analysis", IEEE Trans. Appl. Supercond., Vol. 28, No. 3, 2017, p. 1.

[27] Kundrata, J., Merzel, F., and Arsoski, S., "Design of Magnetic Shielding from Space Radiation using Numerical Methods," 42nd International Convention on Information and Communication Technology, Electronics, and Microelectronics (MIPRO), 2019, p. 133.

[28] Ambroglini, F., Battiston, R., and Burger, W.J., "Evaluation of superconducting magnet shield configurations for long-duration manned space missions," Front. Oncol., Vol. 6, 2016, p. 97

[29] Desiati P. and D'Onghia E., "CREW HaT: A magnetic shielding system for space habitats," 51st International Conference on Environmental Systems, Saint Paul, MN, 2022, https://ttu-ir.tdl.org/items/c90cff0d-ebd0-483a-8321-4fc7f3a9f0d1, https://arxiv.org/abs/2209.13624.

[30] Masi, James. (2013). "Overview of Halbach magnets and their applications.", Electrical Manufacturing and Coil Winding Expo 2010-2013. 134-139.

[31] SuperPower Inc., https://www.superpower-inc.com/

[32] Ansys® Academic Research Mechanical, Release 18.1, Help System, Coupled Field Analysis Guide, ANSYS, Inc.

[33] Advanced Conductor Technologies LLC, https://www.advancedconductor.com.

[34] Y. Iwasa, *Case Studies in Superconducting Magnets: Design and Operational Issues*. Springer, 2009. [Online]. Available: http://ebookcentral.proquest.com/lib/ wisc/detail.action?docID=437907.

[35] C. Haese, *et al.* "Active Magnetic Shielding Final Report – EMA 596 Spring 2021" *University of Wisconsin – Madison Department of Engineering Physics*, May 27, 2021.

[36] P.M. O'Neill Tcs S. Golge (2015). Badhwar - O'Neill 2014 Galactic Cosmic Ray Flux Model Description. Houston, Texas: NASA. Available:
https://spaceradiation.larc.nasa.gov/nasapapers/TP-2015-218569.pdf

[37] P. Lee. "Ybco critical surface." (2009), [Online].
Available:
https://nationalmaglab.org/images/magne_development/asc/plots/YBCO_CritSurf_1280x864-pal256.png.

[38] "2G HTS Wire." (2012), [Online]. Available:
http://www.superpower-inc.com/content/2g-hts-wire.

[39] D. Hazelton, "2g HTS properties beyond critical current," 2013.

[40] D. C. van der Laan, J. D. Weiss, and D. M. McRae, "Status of corc® cables and wires for use in high-field magnets and power systems a decade after their introduction," 2019. [Online]. Available: https://iopscience.iop.org/article/10.1088/0953-2048/30/1/014002/ampdf.

[41] J. Weiss, T. Mulder, H. J. ten Kate, and D. C. van der Laan, "Introduction of corc® wires: Highly flexible, round high-temperature superconducting wires for magnet and power transmission applications," 2017. [Online]. Available:
https://iopscience.iop.org/article/10.1088/0953-2048/30/1/014002/ampdf.

[42] A. Otsuka, T. Kiyoshi, and M. Takeda, "A 1.3 GHz NMR magnet design under high hoop stress condition," 2010. [Online]. Available: https://ieeexplore.ieee.org/document/5443602.

[43] "Hexcel carbon fiber datasheet." (2024), [Online]. Available:
https://www.hexcel.com/Resources/DataSheets/Carbon-Fiber.

[44] J. van Nugteren, "Normal zone propagation in a YBCO superconducting tape," 2012. [Online]. Available: https://essay.utwente.nl/62096/1/MSc_J_van_Nugteren.pdf.

[45] M. Marchevsky, "Quench detection and protection for high-temperature superconductor accelerator magnets," 2021. [Online]. Available: https://www.mdpi.com/2410-390X/5/3/27.

[46] Solidworks, https://www.solidworks.com.

[47] Y. Iwasa, "Hts magnets: Stability; protection; cryogenics; economics; current stability/protection activities at FBML," 2003. [Online]. Available:
https://www.sciencedirect.com/science/article/pii/S0011227503000468.

[48] H. Maeda and Y. Yanagisawa, "Recent developments in high-temperature super-conducting magnet technology," 2014. [Online]. Available: https://ieeexplore.ieee.org/document/6649987.

[49] R. Teyber, M. Marchevsky, S. Prestemon, J. Weiss, and D. van der Laan, "Corc cable terminations with integrated hall arrays for quench detection," 2020. [Online]. Available: https://iopscience.iop.org/article/10.1088/1361-6668/ab9ef3.

[50] G. Nellis and S. Klein, *Introduction to Engineering Heat Transfer*. Cambridge University Press, 2020.

[51] D. Laan, J. Weiss, and D. McRae, "Recent CORC progress," 2018.

[52] https://www.creare.com.

[53] Private communication with Mark Zagarola of Creare, July 2022.

[54] T. Steiner, "Looped Thermoacoustic Cooler with Self-Circulating Large Area Cooling," *Cryocoolers 22*, pp. 479-488 (2023).

[55] https://www.shicryogenics.com.

[56] E.A. Al Ali, "Introduction to Engineering: Biomimetic Design," Penn State, 2014.

[57] ICRP, 2009. Adult Reference Computational Phantoms. ICRP Publication 110. Ann. ICRP 39.

[58] https://www.nasa.gov/missions/artemis/orion/orion-passengers-on-artemis-i-to-test-radiation-vest-for-deep-space-missions.

[59] http://w3.iihe.ac.be/~aguilar/PHYS-467/PA3.html.

[60] Recent Developments in Geant4, J. Allison et al., Nucl. Instrum. Meth. A 835 (2016) 186-225.

[61] Geant4 Developments and Applications, J. Allison et al., IEEE Trans. Nucl. Sci. 53 (2006) 270-278.

[62] Geant4 - A Simulation Toolkit, S. Agostinelli et al., Nucl. Instrum. Meth. A 506 (2003) 250-303.

[63] CERN, https://home.cern.

[64] Singleterry, R.C., Blattnig, S.R., Clowdsley, M.S., Qualls, G.D., Sandridge, C.A., Simonsen, L.C., Slaba, T.C., Walker, S.A., Badavi, F.F., Spangler, J.L., Aumann, A.R., Zapp, E.N., Rutledge, R., Lee, K., Norman, R.B., Norbury, J.W., OLTARIS: On-Line Tool for the Assessment of Radiation in Space. Acta Astronautica, Volume 68, pp. 1086-1097 (2011).

[65] OLTARIS Web-Tool: https://oltaris.nasa.gov.

[66] Desiati, P. and Zweibel, E.G.: 2014, The Astrophysical Journal 791, 51. doi:10.1088/0004-637X/791/1/51.

[67] NASA 2023. NASA Spaceflight Human-System Standard Volume 1, Crew Health. NASA-STD-3001.

[68] ICRP, 2010. "Conversion Coefficients for Radiological Protection Quantities for External Radiation Exposures." ICRP Publication 116, Ann. ICRP 40(2-5).

[69] Cucinotta, F.A.; Durante, M. Evidence Report: Risk of Radiation Carcinogenesis; National Aeronautical and Space Agency: Houston, TX, USA, 2013.

[70] Cucinotta, F.A.; Wang, H.; Huff, J.L. Evidence Report: Risk of Acute or Late Central Nervous System Effects from Radiation Exposure; National Aeronautical and Space Agency: Houston, TX, USA, 2013.
[71] Wu, H.; Huff, J.L.; Casey, R.; Kim, M.H.; Cucinotta, F.A. Evidence Report: Risk of Acute Radiation Syndromes Due to Solar Particle Events; National Aeronautical and Space Agency: Houston, TX, USA, 2013.